

# **Understanding the nanoscale structure of hexagonal phase lyotropic liquid crystal membranes**

Benjamin J. Coscia,<sup>†</sup> Joe Yelk,<sup>†</sup> Matthew A. Glaser,<sup>†</sup> Douglas L. Gin,<sup>‡,¶</sup> Xunda Feng,<sup>§</sup> and Michael R. Shirts<sup>\*,‡</sup>

<sup>†</sup>*Department of Physics, University of Colorado Boulder, Boulder CO, 80309, USA*

<sup>‡</sup>*Department of Chemical and Biological Engineering, University of Colorado Boulder,  
Boulder, CO 80309, USA*

<sup>¶</sup>*Department of Chemistry and Biochemistry, University of Colorado Boulder, Boulder CO  
80309, USA*

<sup>§</sup>*Department of Chemical and Environmental Engineering, Yale University, New Haven,  
Connecticut 06511, USA*

E-mail: michael.shirts@colorado.edu

## Abstract

Nanostructured porous membranes made from the cross-linked hexagonal phase of self-assembled lyotropic liquid crystals (LLCs) are a promising material for selective separations. In this work, we investigate an experimentally characterized LLC membrane using atomistic molecular modeling. In particular, we compare simulated X-ray diffraction (XRD) patterns with experimental XRD to quantify and understand the differences between simulation and experiment. We find that pores are likely composed of 5 columns of stacked LLC monomers which surround each hydrophilic core. We learned that these columns likely move independently of each other over time scales which we can not simulate. We find that some of the structure previously attributed to monomer tail tilt is likely instead due to ordered tail packing. Although this system has been reported as dry, we show that small amounts of water are necessary to fully reproduce all features from the experimental XRD pattern due to asymmetries introduced by hydrogen bonds between monomer head groups and water molecules. We explore the composition and structure of the nanopores and reveal that there exists a composition gradient rather than an abrupt partition between the hydrophilic and hydrophobic regions. A caveat is that the time scales of the dynamics are extremely long for this system, resulting in simulated structures that appear too ordered which requires careful examination of the metastable states observed in order to draw any conclusions. The clearer picture of the nanoscopic structure of these membranes provided in this study will enable a better understanding of the mechanisms of small molecule transport within these nanopores.

## 1 Introduction

More highly selective nanoporous membranes would be extremely useful in order to perform complex aqueous separations with seawater and various sources of wastewater. Sodium chloride and boron in seawater,<sup>1</sup> and organic micropollutants found in municipal and industrial wastewaters<sup>2</sup> are examples of the diverse constituents of these water sources. By efficiently

separating contaminants from feed solutions with highly selective membranes, it is possible to reduce the number of required membrane passes and post-treatment steps needed for a given filtration process,<sup>3</sup> thus lowering energy requirements. Additionally, one can extract valuable resources from the feed streams. For example, flowback water produced during hydraulic fracturing of shale formations contains dissolved species such as acetate whose extraction has economic value.<sup>4</sup>

Reverse osmosis (RO) and nanofiltration (NF) are two prevailing membrane filtration processes that can be used to separate solutes on the order of 1 nm in size and smaller, as well as ions. However the porous architecture of commercially available membranes lack uniformity which severely impacts their selectivity.<sup>5</sup> Although scalable, their fabrication involves the spontaneous assembly of polymers into disordered structures which offer separation pathways that are tortuous and polydisperse in size.<sup>3</sup> Tortuosity increases the effective length that a solute must travel, while polydispersity limits membrane selectivity.

Nanostructured porous membrane materials have become an increasingly popular research area for aqueous separations applications because they offer the ability to control pore architecture at the molecular scale, thereby permitting the design of solute-specific separation membranes.<sup>6</sup> However their development has been limited by the ability to synthesize and scale various technologies. Graphene sheets are atomically thick which results in excellent water permeability but defects during manufacturing severely impact selectivity.<sup>7</sup> Molecular dynamics (MD) simulations of carbon nanotubes show promise,<sup>6</sup> but synthetic techniques are unable to achieve scalable alignment and pore monodispersity.<sup>8,9</sup> Consequently, there is a need for a scalable nanostructured porous membrane.

Preliminary evidence has shown that crosslinked lyotropic liquid crystal (LLC) membranes are scalable and may be capable of performing highly selective separations. LLCs are amphiphilic molecules that have the ability to self-assemble into porous nanostructures<sup>10</sup> and can be crosslinked to create mechanically strong membrane films with pores on the order of 1 nm in diameter.<sup>11</sup> Unlike most commercial NF membranes, LLC membrane pores are

uniform in size because they are self-assembled. Since LLC membranes lack a pore size distribution, they inherently exhibit high selectivity due to their strict molecular weight cut-off (MWCO).<sup>11</sup> Additionally, the LLC monomers examined in this paper are salts, and therefore lead to Donnan exclusion of ions in solution. The membrane gains a net surface charge when counterions from the head groups that line the pore walls escape into the feed solution in an effort to balance the gradients of concentration and electric potential.<sup>12</sup>

The feasibility of nanostructured LLC membranes for selective separations has been demonstrated using LLCs that form the type 1 bicontinuous cubic ( $Q_I$ ),<sup>13-15</sup> and the inverted hexagonal ( $H_{II}$ )<sup>11</sup> phases. When separating organic solutes from NaCl,  $Q_I$  phase membrane filtration experiments have shown selectivity 2–3 times higher than commercial RO and 6–12 times higher than commercial NF membranes.<sup>4</sup> When separating a series of various sized dyes, the  $H_{II}$  phase membrane showed complete rejection of dyes bigger than 1.2 nm in size.<sup>11</sup>

The  $H_{II}$  phase pore geometry (Figure 1) has a higher theoretical capacity for transport than the  $Q_I$  phase. The  $H_{II}$  phase forms at room temperature in the presence of c.a. 10 wt% water and consists of hexagonally packed, hydrophilic pore columns.<sup>10</sup> In the absence of water, neat monomer will form the same hexagonal columnar structure which, in literature, has been referred to as the  $Col_h$  thermotropic phase.<sup>16</sup>  $Q_I$  phase membranes consist of a tortuous network of three dimensionally interconnected pores that prevent optimal through-plane transport. In contrast, the densely packed, non-tortuous and uniform sized pores of  $H_{II}$  phase membranes represent the ideal geometry for achieving high solute flux.<sup>17</sup> However, the hexagonally packed liquid crystalline domains of the  $H_{II}$  phase generally form isotropically oriented and therefore mutually unaligned domains which are detrimental to membrane permeability. This domain scale misalignment had inhibited further development of this technology, and research efforts were focused on the  $Q_I$  phase, whose geometry does not require alignment.<sup>18</sup>

However, recently researchers have learned how to macroscopically align the hexagonal

domains which has revived research into  $H_{II}$  phase LLC membranes. In 2014, Feng et al. showed that one can align  $Col_h$  hexagonal domains, created by the monomer Na-GA3C11, using a magnetic field with subsequent cross-linking to lock the structure in place.<sup>16</sup> In 2016, Feng et al. showed that one could obtain the same result by confining neat monomer between PDMS or glass substrates since hexagonal mesophases preferentially anchor perpendicular to both surfaces.<sup>19</sup> Current experimental efforts are focused on extending the method to the  $H_{II}$  phase and characterizing the performance of these newly aligned systems.

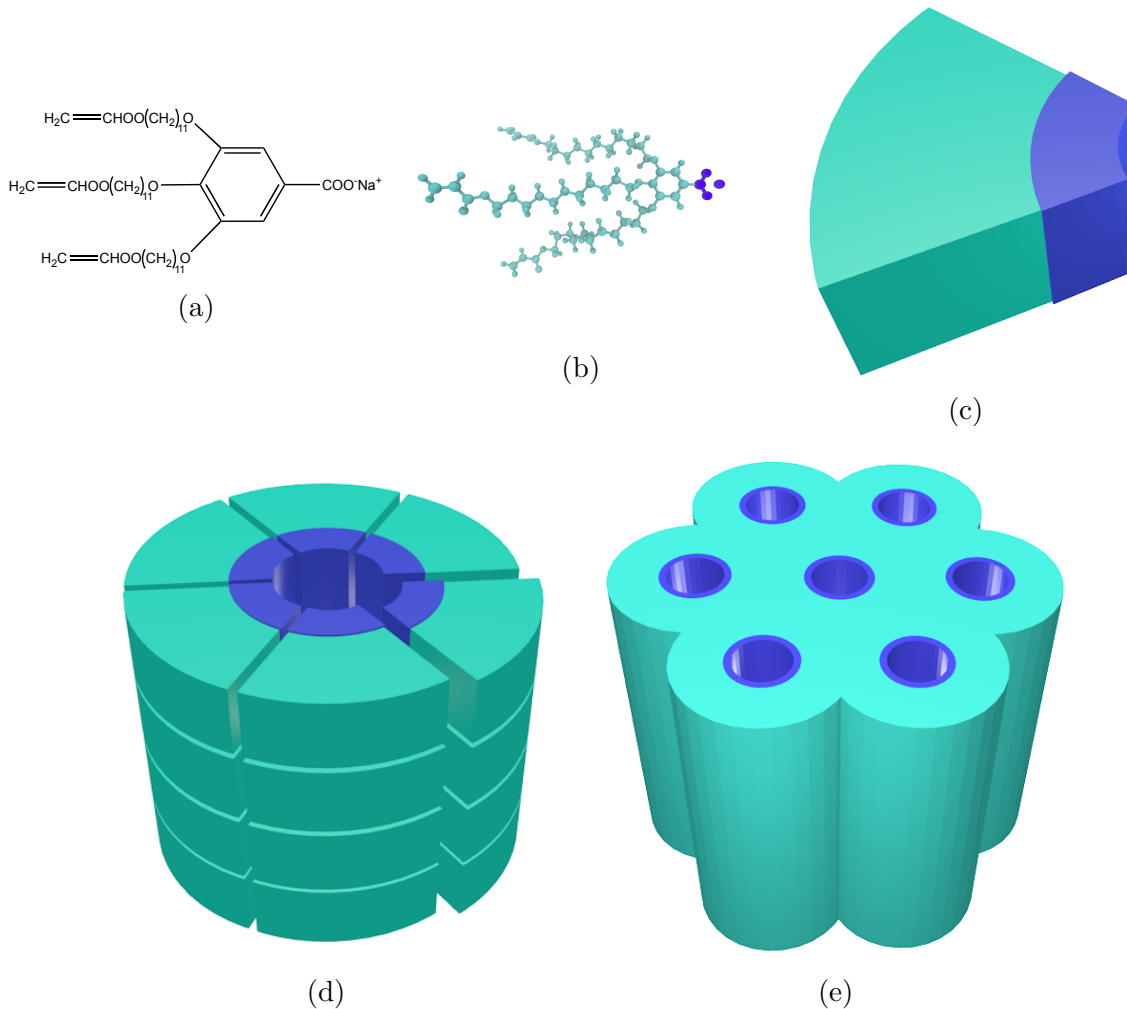


Figure 1: (a) The LLC monomer Na-GA3C11 (b) rendered atomistically (c) exhibits wedge-like character. (d) Monomers stack on top of each other to create columns with short range order then assemble into pores with hydrophilic head groups (blue) face towards the pore center. (e) The pores assemble into hexagonally packed columnar mesophases.

Our current understanding of the molecular details of LLC membranes' nanostructure is not sufficient to be able to precisely design them for specific separations. Dischinger et al. attempted to use an empirical model that correlates the physiochemical properties of the counterion used in a Q<sub>I</sub> phase LLC membrane to solute rejection.<sup>20</sup> Although their model showed some qualitative agreement with experiment, the quality of fit of their model was limited due to complex solute-membrane interactions which could not easily be modeled. Additionally, they observed an unexpected discrepancy in the relationship between uncharged solute rejection and water permeability which will require a more in-depth knowledge of the difference between solute and solvent transport.

Over the past 20 years, H<sub>II</sub>-phase LLC polymer membrane studies have been limited primarily to Na-GA3C11 with some characterization done after minor structural modifications. Resel et al. varied the length of the monomer tails and the counterion used and observed its effect on pore spacing.<sup>21</sup> In a later study of rejection performance, it was shown that membranes formed by cross-linked Na-GA3C11 in the H<sub>II</sub> phase cannot separate solutes less than 1.2 nm in diameter because the pores are too large.<sup>11</sup> We do not yet understand how to controllably reduce the effective pore size or how to tune the chemical environment in the nanopores of this or related materials for small molecule separations. The only source of predictive modeling for LLC systems have been macroscopic models that likely do not adequately describe transport at these length scales.<sup>13</sup> Modeling with molecular detail could provide sufficient information about the mechanisms and chemical features to better inform experimental design of similar nanostructured membranes.

A molecular-level understanding of LLC membrane structure, enabled by molecular dynamics (MD) simulations, can provide guidelines to reduce the large chemical space available to design monomers for creation of separation-specific membranes. Useful molecular-level modeling should incorporate a detailed picture of the nanoscopic pore structure which is crucial to understanding the role of monomer structure in solute transport and membrane design. Atomistic molecular dynamics simulations can provide the required level of detail

(Figure 2), assuming the force fields are sufficiently accurate. With such an atomistic model, we can directly observe molecular-level solute transport and suggest governing mechanisms. We can observe how the choice of head group interacts with solutes of interest. We can interchange counterions which may influence both the pore size and the strength of the Donnan potential.

In this study, we achieve a more realistic atomistic description of LLC membranes than, to our knowledge, has ever previously been created, and explore what new structural information can be gained and what structure hypotheses are supported by this model. We validate the results using as much experimental information as possible. We are most interested in reproducing the conclusions about structure drawn from small angle X-ray scattering (SAXS) and wide angle X-ray scattering (WAXS) experiments as well as in matching ionic conductivity measurements.<sup>19</sup>

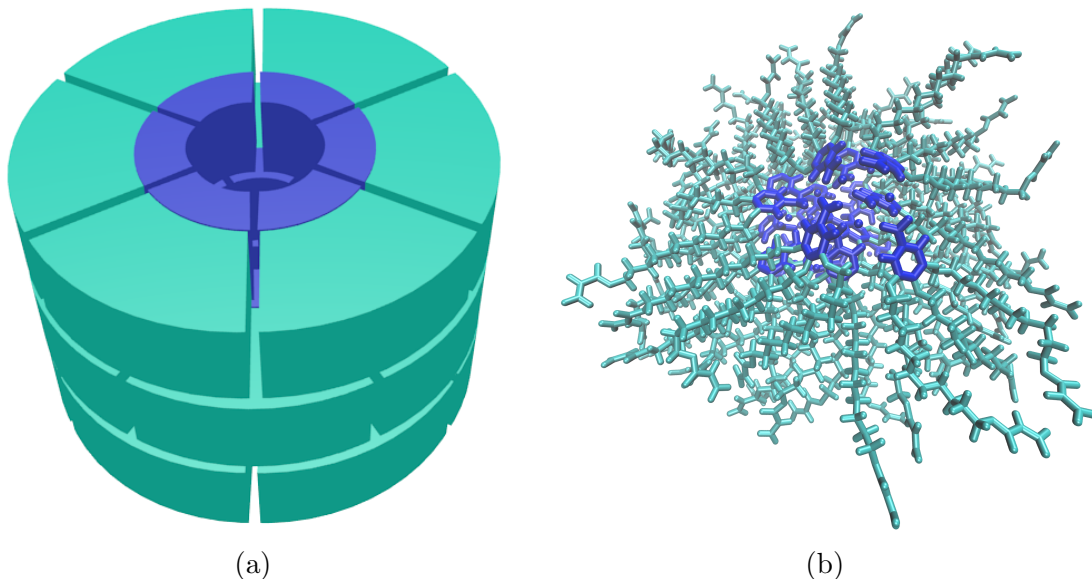


Figure 2: (a) Previous understanding of the pores are essentially speculations based on limited chemical and experimental data. (b) We use detailed molecular modeling in this paper in order to appropriately model the pore's complex architecture which is crucial to understanding the mechanism of solute transport. In both pictures, the head group region is colored blue and the tail region is colored cyan.

In this paper, we perform molecular modeling of the Col<sub>h</sub> assembly formed by Na-GA3C11. Compared to the H<sub>II</sub> phase, the Col<sub>h</sub> phase is a simpler starting point. The system is not assembled in aqueous phase which allowed us to simulate longer timescales, and there exists detailed experimental characterization of the fully aligned state, including 2D wide-angle X-ray scattering (WAXS) patterns (Figure 3a) which are useful for reconstructing structural data.

There are five major features of interest present in the 2D experimental pattern shown in Figure 3a.

1. *R- $\pi$* : The location of the first is at  $q_z = 1.7 \text{ \AA}^{-1}$ , corresponding to a real space separation of 3.7 Å. Previous work attributes this reflection to  $\pi$ - $\pi$  stacking between aromatic rings in the direction perpendicular to the membrane plane, or z-axis.<sup>16</sup> For simplicity, we will refer to this reflection as R- $\pi$ .
2. *R-double*: A weak intensity line, located at exactly half the  $q_z$  value of R- $\pi$  ( $q_z = 0.85 \text{ \AA}^{-1}$ ), corresponds to real space periodicity of 7.4 Å. Since this reflection corresponds to double the spacing of R- $\pi$  in real space, we will refer to it as R-double. R-double has been previously interpreted as  $2_1$  helical ordering of aromatic rings along the  $z$  axis.<sup>16</sup>
3. *R-alkanes*: A low intensity ring located at  $|\mathbf{q}| = 1.4 \text{ \AA}^{-1}$  marks the third major reflection of interest. The real space separation corresponds to 4.5 Å which is characteristic of the average spacing between packed alkane chains.<sup>22</sup> We will call this reflection R-alkanes.
4. *R-spots*: Within R-alkanes, are four spots of higher relative intensity. Accordingly, we name these reflections R-spots. The location of all spots is  $\sim 37^\circ$  from the  $q_z$  axis in their respective quadrants. In many liquid crystal systems one can explain the spots as the product of alkane chains tilted with respect to the membrane plane.<sup>23</sup>
5. *R-pores*: The final feature corresponds to the spacing and symmetry of the pore columns. The feature, which we named R-pores, is characterized by reflections along

the equatorial axis defined by  $q_z = 0$ . The spacing between dots is indicative of the hexagonal symmetry of the packed pores, and the location of the leading peak (closest to  $q_r = 0$ ) is related to the distance between pores. We observe the same information with higher resolution by looking at the same system's 1D SAXS pattern (Fig. 3b).

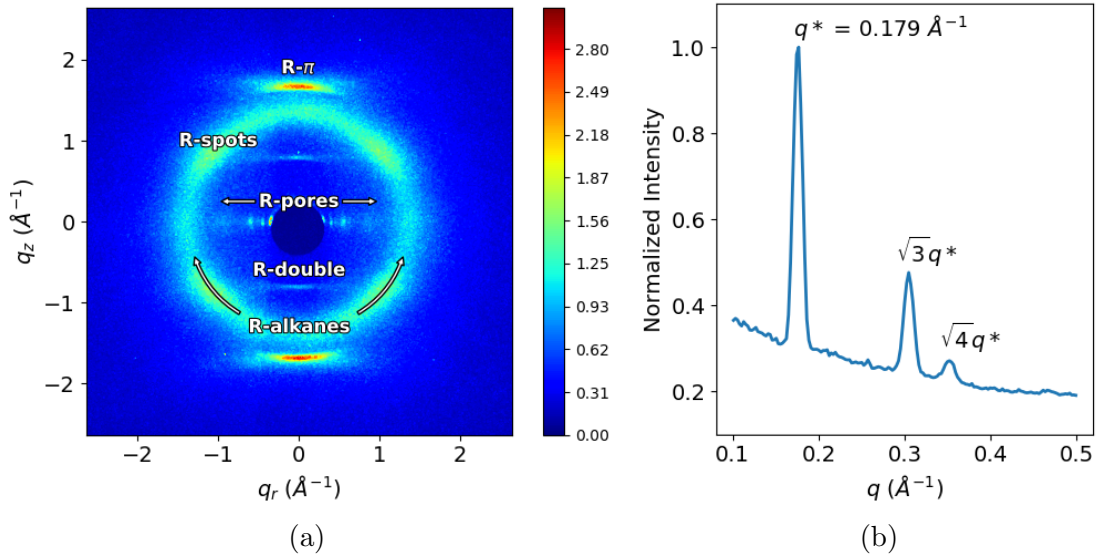


Figure 3: (a) 2D WAXS gives details about repeating features on the order of angstroms. Experimentalists have explained each of the 5 major reflections present as follows: (R- $\pi$ ) Aromatic head groups  $\pi - \pi$  stack 3.7  $\text{\AA}$  apart. (R-double) Monomers arrange vertically in a  $2_1$  helix. (R-alkanes) Alkane chain tails pack 4.5  $\text{\AA}$  apart. (R-spots) Monomer tails are tilted with respect to the membrane plane. (R-pores) As derived from SAXS, the pores are spaced 4.12 nm apart and pack hexagonally (b) (Reproduced from 19) The repeat spacing in the 1D small angle X-ray scattering pattern is characteristic of hexagonal packing. The leading peak,  $q^*$ , represents the distance between the  $d_{100}$  planes. Using this distance, we know that the distance between pore centers is 4.12 nm.

Despite having structural data, there is still information which experiment cannot definitively answer. Specifically, we want to know:

1. What is the density of monomers that pack around each hydrophilic core?

Authors often describe this and similar systems as being made up of layers. A simple molecular simulation study of a similar molecule suggested that there are 4 monomers in each layer. Their estimation is based on a simulated system containing only 16 total monomers which likely does not sufficiently model the chemical environment present

in the real system.<sup>24</sup> A separate calculation based on the volume of the liquid crystal monomers proposes that there are seven monomers in each layer.<sup>21</sup>

We are careful to avoid the term “layers” since many liquid crystalline systems have long range order in 1 or 2 spatial dimensions and short range order in the other dimensions.<sup>25</sup> In the system we are studying, there are long-range 2D correlations in the hexagonal array of pores (xy plane) and short range z-direction correlations between stacked columns of monomers. In this study, we use atomistic molecular modeling to study how the system’s structure is affected by the density of these monomer columns that surround each pore’s hydrophilic core.

## 2. What structural motif best matches experimental 2D WAXS patterns?

On the short timescales accessible to MD (even the 100’s of nanoseconds of simulation performed here are short compared to experimental timescales), we observe distinct metastable configurations which depend on starting configuration. We simulated XRD patterns of our system and compared them to experimental 2D WAXS patterns (Figure 3a) so that we ensure our model creates a nanoscopic chemical environment maximally consistent with experiment within the constraints of our forcefield. Using this approach, we are able to confirm some previous interpretations of the WAXS pattern and refute others.

## 3. Is it necessary to include any water in order to appropriately model the Col<sub>h</sub> phase?

While the Col<sub>h</sub> phase is described as dry, it is likely that small amounts of ambient water are absorbed into the system. The hydrogen bonding network formed by the water may play a role in structuring the pore. We used simulated X-ray diffraction (XRD) patterns to uncover any meaningful structural difference between a “dry” and a “wet” system.

## 4. What is the detailed atomistic structure of the pores?

The limited picture that experiment provides tells us that there are hexagonally packed, hydrophilic regions where transport is likely to occur. One may instinctively imagine these regions as tube-like pathways with well-defined boundaries. We explored the composition of the pores, the partition between the hydrophilic and hydrophobic regions, and its sensitivity to initial configuration, including both dry and wet systems.

## 2 Methods

### 2.1 Monomer Parameterization

We parameterized the interaction potential for the liquid crystal monomer Na-GA3C11 using the Generalized AMBER Force Field (GAFF)<sup>26</sup> with the Antechamber package<sup>27</sup> provided with AmberTools16.<sup>28</sup> We assigned atomic charges using the am1bccsym method of `molcharge` shipped with QUACPAC from Openeye Scientific Software. We ran all molecular dynamics simulations using GROMACS 2016.<sup>29–32</sup>

We generated an ensemble of characteristic, low-energy vacuum monomer configurations by applying a simulated annealing process to a parameterized monomer. We cooled monomers from 1000K to 50K over 10 nanoseconds. We randomly pulled a low energy configuration from the trajectory then reassigned charges using `molcharge`. Using the new charges, we annealed the monomer system again and pulled a random monomer configuration from the trajectory which we used for full system construction (Figure 4a). See section S-1 for further detail of the parameterization process.

### 2.2 Unit Cell Preparation

The timescale for self-assembly of monomers into the hexagonal phase is unknown and likely outside of a reasonable length for an atomistic simulation, calling for a more efficient way to build the system. Previous work has shown a united-atom model self assemble into the H<sub>II</sub> phase configuration in ∼1000 ns.<sup>33</sup> We attempted atomistic self-assembly by packing

monomers into a box using Packmol.<sup>34</sup> Simulations of greater than 100 ns show no indicators of progress towards an ordered system (see section S-2). To bypass the slow self-assembly process, we use Python scripts to assemble monomers into a structure close to one of a number of hypothesized equilibrium configurations (Figure 4). These initial structures may result in equilibration into slowly-interconverting metastable states, an issue we will address later in the paper.

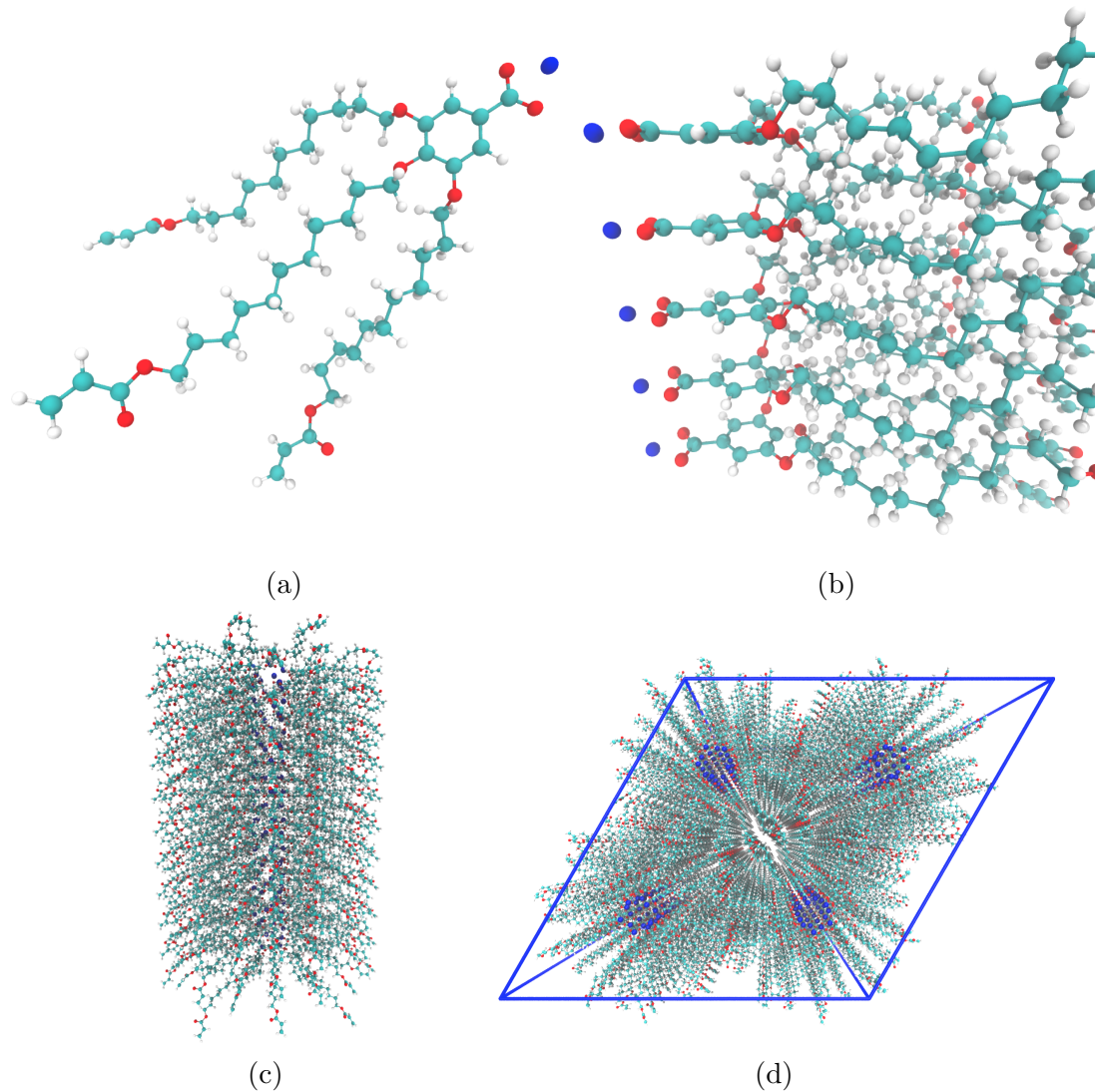


Figure 4: (a) We parameterized a single monomer and annealed it to produce a low energy configuration. (b) We assembled monomers into columns by stacking them on top of each other. (c) We duplicated each column and rotated them to create hydrophilic pore centers. We chose to stack twenty monomers into each column. (d) We duplicated the pores and placed them into a monoclinic unit cell with hexagonal symmetry.

A typical simulation volume contains four pores in a monoclinic unit cell, the smallest unit cell that maintains hexagonal symmetry when extended periodically. Each pore is made of columns of stacked monomers with periodic continuity along the pore axis, avoiding any edge effects and creating an infinite length pore ideal for studying transport. We prefer a small number of stacked monomers in order to reduce computational cost and to allow us to look at longer timescales. Ultimately, we chose to build a system with 20 monomers per column in order to minimize finite size effects with reasonable computational expense and to obtain sufficient resolution when simulating XRD patterns (see further discussion in section S-3).

### 2.3 Monomer Placement

When constructing an initial configuration, there are a number of variables which require careful consideration while placing monomers. The equilibrium configuration is sensitive to some while insensitive to others. We find the starting pore radius, defined as the distance of a chosen head group carbon from the pore's central axis, does not influence the equilibrium structure if one chooses a reasonable value. The pore radius is chosen to be 0.5 nm in our initial configurations. The initial distance between pores, within a wide range, also has little effect on the equilibrated structure. However, one should not start them too close or there will be high energy repulsions during early equilibration. We chose an initial pore spacing of 4.5 nm,  $\sim$ 10% larger than the experimental value of 4.12 nm. A sensitivity analysis of both parameters is presented in the Supporting information, section S-4. The distance between vertically stacked monomers, the xy position of monomers with respect to vertically adjacent monomers, and the number of columns per pore do influence the equilibrated structure and require further justification for their choices. We rely on experimental data to inform them.

We chose the vertical spacing between monomers for the initial configuration based on R- $\pi$  and then allowed the system to readjust during equilibration. We rotated each monomer so the plane of its aromatic head group would be coplanar with the xy plane. We explored

three different initial monomer spacings. The first is exactly equal to  $R-\pi$  with monomers placed so aromatic rings stack 3.7 Å apart in the  $z$ -direction. We also extensively explored a second system with an initial spacing of 5 Å. We briefly explored a third system with an initial spacing of 10 Å. However this largest spacing yields non-physical behavior which is detailed in the Supporting Information, section S-4.3.

We chose the relative orientation between vertically adjacent monomers in each column based on clues from diffraction data as well as the various known stacking modes of benzene and substituted benzene rings: sandwiched, parallel-displaced and T-shaped.<sup>35</sup> We ruled out the T-shaped configuration because its ~5 Å equilibrium stacking distance<sup>35</sup> is inconsistent with  $R-\pi$ . It is also infeasible for the monomers to orient in the T-shaped conformation because of the bulky tail groups. We explored the system's preference towards the sandwiched vs. parallel displaced stacking modes in some detail. Both have reported stacking distances near the  $R-\pi$  value of 3.7 Å. Head groups in our sandwiched initial configuration stack directly on top of each other while head groups in the parallel displaced initial configuration stack with an offset of  $180^\circ/ncol$  where  $ncol$  is the number of columns per pore. See Figure S-8 for a detailed illustration of the initial configurations in each mode.

The number of columns per pore is unknown, as stated in Question (1). We tested configurations constructed with a varied number of columns per pore. We built systems in the sandwiched and parallel displaced configurations with 4, 5, 6, 7 and 8 monomers per layer.

## 2.4 Equilibration

We developed equilibration schemes for creating dry and wet configurations. Both schemes start with an initial configuration generated according to the previous guidelines. For wet systems, we added the desired concentration of water to the initial configuration and carried out equilibration in the same way as the dry systems. First, we fixed monomer head groups in place using position restraints with a force constant of  $10^6$  kJ mol<sup>-1</sup> nm<sup>-2</sup>. We gradually

released the position restraints by decreasing the force constants over a series of NVT simulations. We allowed the resulting unrestrained structure to equilibrate for 5 ns in the NPT ensemble with pressure controlled by the Berendsen barostat followed by NPT equilibration simulations run for at least 400 ns using the Parrinello-Rahman barostat. More equilibration details are given in section S-6.

## 2.5 Equilibrium Calculations

### 2.5.1 *Determining equilibration time*

Using equilibrated structures, we carried out various calculations to characterize the system. We defined the point at which a system is equilibrated based on when the distance between pores stopped changing. We determined when the distances stopped changing by applying the statistical test of Chodera,<sup>36</sup> implemented as `pymbar.timeseries.detectEquilibration`, to the time series. Typically, the pore-to-pore distance equilibrated between 200 and 350 ns. We used data collected after equilibration to do all subsequent analysis.

### 2.5.2 *Calculation of pore spacing*

To calculate the equilibrated pore spacing, we measured the distance between pore centers. We located the pore centers by averaging the coordinates of sodium ions in their respective pores. We generated pore spacing statistics using the bootstrapping technique (See section S-7 of the Supporting Information). The pore spacings calculated in this way are consistent with one half of the *x* and *y* box vectors (See, Table S-2). However our method for their calculation does a better job capturing the spread of pore-to-pore distances.

### 2.5.3 *Generation of simulated X-ray diffraction patterns*

We generated simulated XRD patterns based on atomic coordinates in order to make a direct experimental comparison. We modeled all atomic coordinates as Gaussian spheres of electron density whose maximum and width are defined by each atom's atomic number

and electronic radius respectively. A three dimensional Fourier transform of the array of electron density results in a three dimensional structure factor which represents the unit cell in reciprocal space. The experimental WAXS measurement was made using a vertically aligned film whose pores were oriented perpendicular to the direction of the incident X-ray beam. Although the pores are vertically aligned, the crystalline domains are still misaligned with respect to the  $xy$  plane. To account for this, we averaged 2D slices of the structure factor at all angles about  $\mathbf{q} = (0, 0, z)$ .

We normalized all diffraction patterns relative to R-alkanes. We believe that the alkane-alkane density, averaged over all angles, is the feature most likely to be replicated between experiment and simulation, as atomistic alkane parameters are relatively well studied. Other features are dependent on system ordering which is likely to have some dependence on initial configuration. We calculated the average intensity within R-alkanes of the experimental pattern,  $I_{avg}$  and divided all intensities by this value. In this way, the average intensity of R-alkanes was equal to 1. When calculating  $I_{avg}$ , we excluded intensities within  $\pm 30^\circ$  of the meridional axis defined by  $q_r = 0$ , since the simulated patterns differ from experiment in those regions in all cases (See Figure 5a). Specifically, in contrast to the experimental WAXS pattern, R- $\pi$ , as it appears in the simulated diffraction patterns, intersects with R-alkanes (See Figure 7). We set an upper bound on the colorbar by multiplying  $I_{avg}$  by a scaling factor,  $f$ . Intensities that appear in the patterns  $\geq f \times I_{avg}$  are colored uniformly. We applied the same scaling method to the simulated patterns. We chose a scaling factor of  $f = 3.1$  in order to visibly display all features in all patterns.

We reported the intensities of R- $\pi$  and R-double by recording the maximum values of the peaks of the  $q_z$  cross-section of the experimental pattern at  $q_r = 0$  (Figure 5b). In the case of the experimental pattern, the peak heights are not perfectly symmetrical, so we report the average of the two heights.

We measured the intensity of R-spots by averaging the peak heights produced by radially integrating the patterns within the R-alkanes region (Figure 5c). In some patterns, the spots

are not easily discernable due to obstruction by other features. In that case, we report the average intensity at the intersection of R-alkanes with the  $q_z$  value of R-double since that is where we expect it to appear based on experiment. Since R-double does not appear in our simulated patterns, we estimate where it should appear as half of the  $q_z$  value of R- $\pi$ .

We measured the intensity of R-pores based on the intensity of the  $d_{100}$  peak (the leading peak closest to  $q_r = 0$ ) of the  $q_r$  cross-section of the patterns at  $q_z=0$  (Figure 5d). The beamstop covers most of the small angle reflections in the experimental 2D WAXS pattern. In order to compare the simulated intensity of R-pores to experiment, we used the  $q_r$  cross-section of 2D SAXS which was generated from the same sample (Figure S-14). Since the  $d_{200}$  peak is partially exposed in the experimental 2D WAXS pattern, we normalized the experimental 2D SAXS cross-section by matching the intensity of the  $d_{200}$  peak between it and the experimental 2D WAXS cross-section. It is possible that the peak is not fully captured in the 2D WAXS pattern and that we have underestimated the intensity of R-pores in the experimental pattern.

#### 2.5.4 *Pair distribution functions and correlation length*

The normalized pair distribution function,  $g(\mathbf{r})$ , describes the probability of finding a pair of particles separated by  $\mathbf{r}$ ,

$$g(\mathbf{r}) = \frac{1}{\rho N} \left\langle \sum_{i=1}^N \sum_{j \neq i}^N \delta(\mathbf{r} + \mathbf{r}_j - \mathbf{r}_i) \right\rangle \quad (1)$$

where  $\rho$  is the average number density of particles and  $\delta(\mathbf{r})$  is the Dirac delta function.<sup>37</sup>

We applied Equation 1 in three dimensions and then extracted one dimensional distribution functions using slices of the grid along the appropriate axis.

We measured the one dimensional pair distribution function,  $g(z)$ , between centers of masses (COM) of aromatic head group rings along the z-axis (perpendicular to the membrane plane). We averaged all 1D  $z$ -directional slices of the full 3D correlation function within

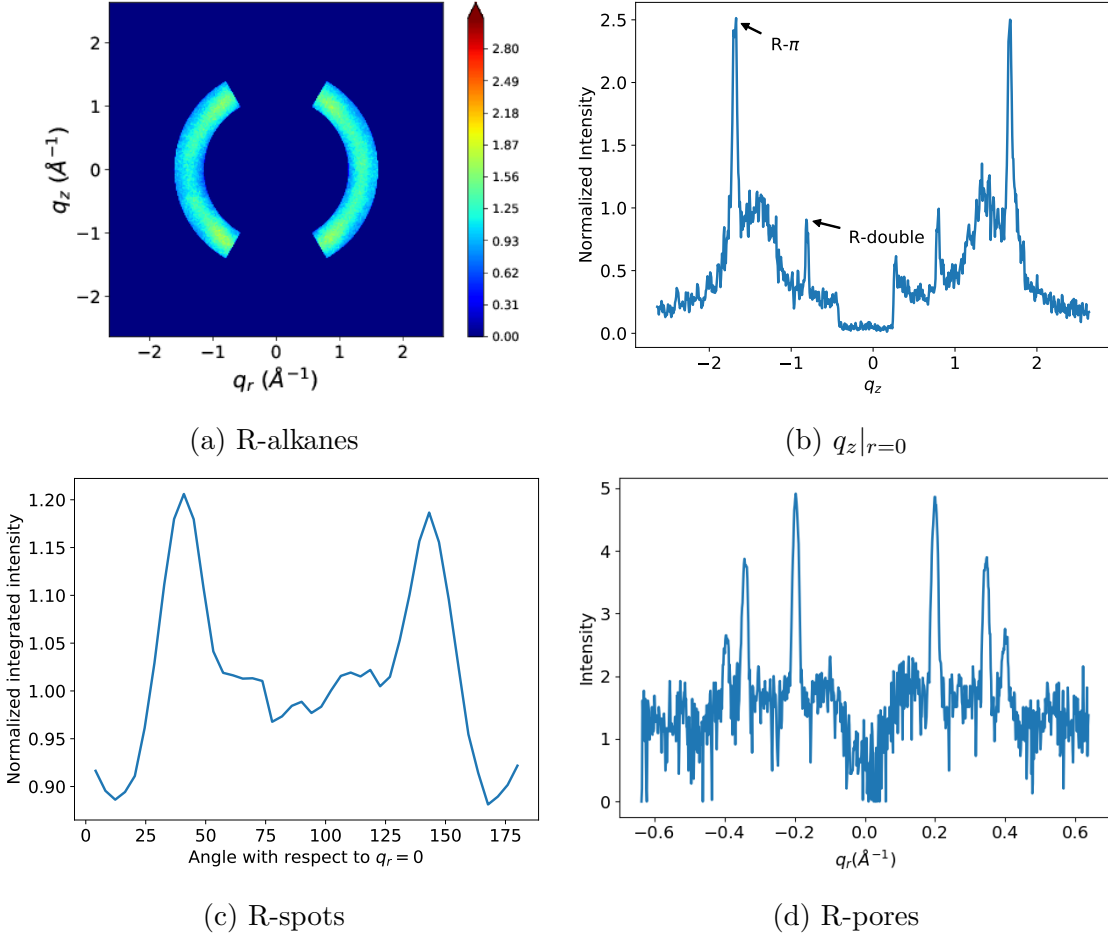


Figure 5: (a) We measured the intensity of R-alkanes by calculating the average intensity within the region bounded by  $|\mathbf{q}| = 1.4 \text{ \AA}^{-1}$  and  $1.57 \text{ \AA}^{-1}$  (between  $4.0$  and  $4.5 \text{ \AA}$  in real space). We excluded intensities within  $\pm 30^\circ$  of the meridional axis defined by  $q_r = 0$ , since the simulated spectra overlap with R- $\pi$  in those regions in all cases. (b) We measured the intensity of R- $\pi$  and R-double based on the peaks of the  $q_z$  cross-section of the diffraction pattern. (c) We measured the intensity of R-spots by averaging the peak heights produced by radially integrating the patterns within the R-alkanes region. We took the intensity of R-spots as the average of the peak intensities near  $-37$  and  $-143^\circ$ . (d) We measured the intensity of R-pores by measuring the height of the  $d_{100}$  peak (the leading peak closest to  $q_r=0$ ) of the cross-section of the diffraction patterns along the  $q_r$  axis at  $q_z=0$ .

$2.1 \text{ \AA}$  of  $(x, y) = (0, 0)$ . We chose  $2.1 \text{ \AA}$  as a crude approximation of the radius of the phenyl ring plane. We calculated the radius as the sum of the longest C-C distance within a phenyl ring ( $2.8 \text{ \AA}$ ) and two times the carbon atom electronic radius ( $0.7 \text{ \AA}$ ).<sup>38</sup>

Here,  $g(z)$  is characterized by an oscillatory function with a period equal to the average distance between stacked monomers, and an amplitude that decays exponentially (see

Figure 10). The rate of decay is related to the correlation length, L, between monomer head groups. We estimated L by fitting the peaks of  $g(z)$ , using the python package `scipy.optimize.curve_fit`,<sup>39</sup> to a decaying exponential function of the form:

$$Ae^{-z/L} \quad (2)$$

where A is a fitting parameter for amplitude, z is the independent variable of  $g(z)$  and L is the fit correlation length. We calculated the error in the estimated value of L as the square root of the diagonal entry of the covariance matrix of optimized fit parameters.

We also used  $g(z)$  to calculate the equilibrated vertical stacking distance between monomers,  $d_{equil}$ . We fit a decaying sinusoidal function (using `scipy.optimize.curve_fit`) to  $g(z)$  of the form:

$$1 - A \cos\left(\frac{2\pi}{d_{equil}}z + B\right) e^{-z/L} \quad (3)$$

where A and B are fit parameters for the function's amplitude and phase shift respectively. This function could be used in place of Equation 2, however it does not consistently fit the peaks of  $g(z)$  from parallel displaced configurations well enough to extract a reliable value of L.

### 2.5.5 Radial distribution functions

We explored the pores' compositions by measuring the average number densities of various monomer components as a function of distance from the pore centers. We looked at the average number density of sodium ions, aromatic rings and carbon atoms making up the monomer tails. We binned the radial distance of all atoms in each group from the pore centers, then normalized by the volume of the annulus defined by the bin edges and the z box vector (See Figure S-13).

## 2.6 Simplified Systems

In order to gain a deeper understanding of discrepancies between the experimental and simulated R- $\pi$  reflection, we used a simplified model where we represent each monomer as a single point scatterer located at the COM of its head group. In order to make a system approximately similar to our equilibrated simulation geometries, we created 4 hexagonally packed pore regions spaced 42.5 Å apart, each with 5 columns of scatterers spaced 4.4 Å apart in the  $z$ -direction. We built the system 4 times taller in the  $z$ -direction (80 scatterers per column) in order to access higher  $q_z$  resolution.

We gave the simplified models the same amount of disorder present in the atomistic simulations. We observe two sources of disorder: thermal motion of atoms and quenched disorder which is created by rapid structural rearrangement during early equilibration and is largely locked into place for the remainder of the simulation. We measured thermal disorder by calculating the standard deviation of the distribution of head group COM positions from their average positions. We measured quenched disorder by calculating the standard deviation of the distribution of head group COMs from their idealized average positions. In the  $z$ -direction, we measured the deviation of the head group COMs from an equally spaced column of head groups. In the  $xy$  plane, we calculated the standard deviation in radial position from the pore center and the angular deviation from equally spaced points surrounding the pore center. This method for calculating quenched order inherently includes thermal disorder.

We approximated interactions between particles by correlating the  $z$ -distance between points within each column of point scatterers. We placed points in each column by drawing random samples from a multivariate normal distribution defined by the mean positions of an equally spaced column of points. We gave the distribution at each point along the column the same standard deviation,  $\sigma_z$ , and we defined a covariance matrix such that the covariance,  $v$ , of the distance,  $d$ , between scatterers decays exponentially from  $v$  according to the equation  $ve^{-d/L}$ , where  $L$  is the correlation length. Unless noted otherwise, we used the experimental

correlation length of 9.0 Å.

We calculated averaged R- $\pi$  profiles by simulating the diffraction pattern of trajectories consisting of 1000 independent simple system configurations generated with point scatterer placement based on the quenched order seen in atomistic simulations. The quenched disorder is greater in magnitude than thermal disorder (See Table 3 in section 3.2.4). This method assumes that the timescales for large scale rearrangements of the system are much longer than what we can feasibly simulate.

## 2.7 Ionic conductivity calculations

We calculated ionic conductivity using the Nernst-Einstein relationship, which relates the DC ionic conductivity,  $\sigma$ , to ion diffusivity,  $D$ , concentration,  $C$ , ion charge,  $q$ , the Boltzmann constant,  $k_b$ , and temperature,  $T$ :

$$\sigma = \frac{q^2 C D}{k_b T} \quad (4)$$

We measured sodium ion diffusion coefficients by calculating the slope of the linear region of the  $z$ -direction mean square displacement curve as indicated by the Einstein relation.<sup>40</sup> We visualized the MSD plot to determine where to begin and end a linear fit. We measured ion concentration with respect to the volume of the entire unit cell. More details are provided in the Supporting Information, Section S-10.

## 2.8 Cross-linking

In order to better match the experimental membrane synthesis process, we created a cross-linking algorithm that one can apply to equilibrated structures. The primary purpose of cross-linking is to create a mechanically robust membrane. For that reason, we are not concerned with replicating the kinetics of the reaction, but instead emphasize understanding how much and in what way cross-linking modulates the system's structure.

We based our cross-linking algorithm on the known reaction mechanism (Figure S-16).

The reaction takes place at the terminal vinyl groups on each alkane tail. The procedure is carried out iteratively. Each iteration, the algorithm chooses carbons to cross-link based on the distance between eligible carbon pairs. The algorithm then updates the topology with the new bonds and atom types, energy minimizes the system and runs a short simulation before selecting the next group of eligible carbons atoms.

## 3 Results and Discussion

### 3.1 Density of monomers around pores

Our simulations best support a model built with 5 monomer columns per pore based on the measured equilibrated pore-to-pore distances. To discern the density of monomer columns in each pore, addressing Question 1 above, we ran simulations of systems created with 4–8 columns per pore. We built systems in both the parallel displaced and sandwiched configurations and equilibrated them according to the dry equilibration procedure. We tested all systems with an initial vertical monomer spacing,  $d$ , of 3.7 Å in accordance with R- $\pi$ . We tested 4 additional systems with monomers initially spaced 5 Å apart vertically (see section 4.1 of the Supporting Information for more details on sensitivity to initial layer spacing). We considered the pore-to-pore spacing to be equilibrated as defined in section 2.5.1. Figure 6 shows the equilibrated pore-to-pore distances for all systems tested.

All systems tested, although equilibrated from the perspective of the metrics used here, are frozen in metastable basins. Not all make physical sense or fit the experimental profile that we are trying to match. In the limit of infinite simulation time, all systems will in theory converge to a single equilibrium configuration, but that time is far beyond the 100's of nanosecond simulated here. For simplicity, we group the systems studied here into the ordered and disordered basins. What we find is that any system where  $d = 3.7$  Å can generally be characterized as being in a more ordered basin, and any system where  $d = 5.0$  Å can be characterized as a more the disordered basin. Generally, when monomers are

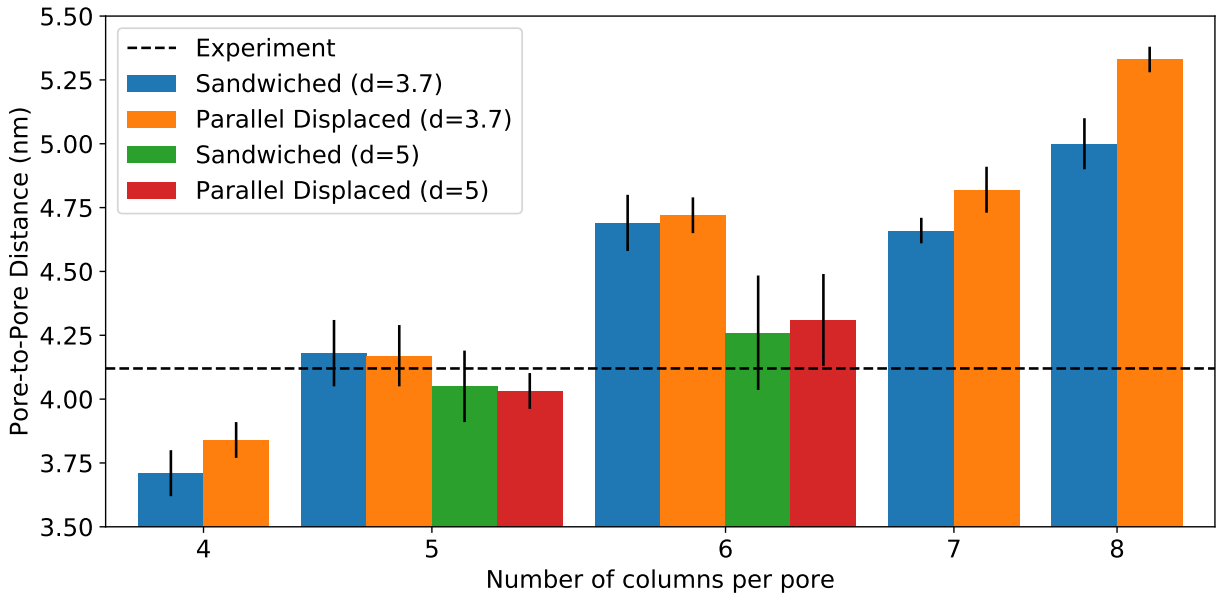


Figure 6: Systems with 5 columns per pore have equilibrated pore spacings closest to the experimental value of 4.12 nm. The equilibrated pore spacing of the model increases as the number of columns in each pore increases.

started further apart, they stay further apart than systems where monomers are started closer together (see Table 2). Because of the extra space between stacked monomers, monomer head groups have more rotational freedom. We quantified the ordering of the head groups using the nematic order parameter (see section S-12 for details of calculation). Disordered basin systems have a lower nematic order parameter (meaning they are more disordered) than ordered basin systems.

Systems built with 5 columns in each pore equilibrate to a pore spacing that is most consistent with the experimental value of 4.12 nm derived from SAXS measurements (Figure 3b). Ordered basin systems built with 4 columns per pore equilibrate to an average pore spacing 0.25 nm lower than experiment. Ordered basin systems built with 6 columns per pore, have an equilibrated pore spacing ca. 0.50 nm higher than experiment. Monomers in disordered basin systems built with 6 columns-per-pore agree with experimental pore-to-pore distances within error, but stack too far apart. Those in the disordered sandwiched and disordered parallel displaced configurations stack  $\sim 4.87$  and  $4.94 \text{ \AA}$  apart respectively,

which is ca. 1.2 Å further apart than suggested by experiment. 5 column-per-pore systems stack, at a maximum, 0.9 Å further apart than experiment (see Table 2). The remainder of this discussion will focus on the analysis of systems built with 5 columns per pore.

### 3.2 Simulated XRD comparison to 2D WAXS data

We can better understand the structure of the system by simulating X-ray diffraction patterns produced from equilibrated MD trajectories (see section 2.5.3) and comparing them to experiment, addressing Question 2. We tested systems built with 5 columns per pore in the parallel displaced and sandwiched configurations at 300 K in the ordered and disordered basins, as those were the most consistent with the most unambiguous X-ray diffraction features, the pore-to-pore spacing and the stacking distance. We generated simulated patterns using the locally equilibrated portion of each simulation trajectory (See Section 2.5.1). There are two important factors to take into account when looking at differences between experimental XRD and simulated XRD. First, the simulated diffraction patterns have some noise, especially along the  $q_z$  axis at  $q_r=0$ , which is where several of the more interesting features are located. This is due to the angle averaging of the 3D structure factor around the  $q_z$ -axis, meaning there are fewer samples as  $q_r$  approaches 0. More importantly, our simulations do not appear to be long enough to sample truly independent configurations within their respective metastable basins (see section 3.4), meaning we must take care in interpreting the results of the XRD. The amount of independent configurations required to converge along the  $q_z$  axis is analyzed in Supporting Information, Section S-13. The simulated patterns generated for all systems studied are shown and compared to experiment in Figure 7.

The simulated XRD patterns show moderate agreement with experiment. There are key qualitative and quantitative differences between the experimental and simulated locations and intensities of each major reflection. The integrated intensity and location of each simulated reflection relative to its experimental counterpart are shown in Table 1. Our approach for measuring the intensity of each reflection is described in Section 2.5.3.

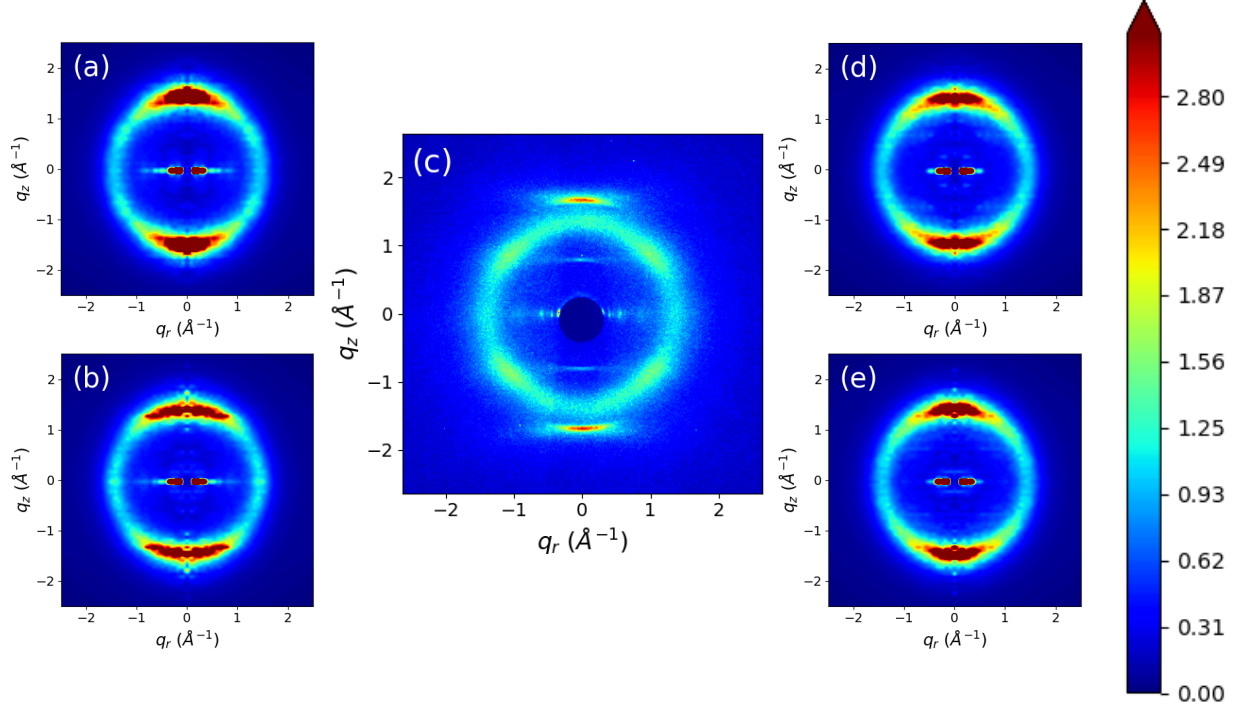


Figure 7: Simulated XRD patterns show some qualitative agreement with experiment. Shown is a comparison of the (a) Sandwiched, ordered basin (b) Sandwiched, disordered basin (d) Parallel displaced, ordered basin and (e) Parallel displaced, disordered basin configurations with (c) experimental WAXS. The major reflections of interest (See Figure 3 for their definitions) are present at varying degrees. In all cases, R-pores, R-alkanes and R- $\pi$  are present to some degree. R-spots is also present, however it is generally partially covered by the broad R- $\pi$  reflection. Quantitative comparisons of the relative intensities and locations of reflections of interest are presented in Table 1. In both XRD patterns generated from parallel displaced patterns, there is a faint line across  $q_z \sim 0.7 \text{ \AA}^{-1}$ , half the simulated value of R- $\pi$ . Although it does not cross through  $q_r = 0 \text{ \AA}^{-1}$ , it is at the same  $q_z$  value where we expect R-double to be present. Still, R-double is not fully reproduced in any of the simulated patterns.

In the next few subsections, we individually address each major reflection, and the similarities and differences between simulation and experiment. We start with relatively uncomplicated analyses of reflections that are very similar between experiment and simulation:

- The location of R-alkanes (section 3.2.1)
- The location and intensity of R-pores (section 3.2.2)

and then move onto more complicated explanations of those reflections whose characteristics

do not match, or have not been fully explained by experiment:

- The origin of R-spots (section 3.2.3)
- The position, shape and intensity of R- $\pi$  (section 3.2.4)
- The origin of R-double (section 3.2.5)

**Table 1:** The simulated XRD patterns of the systems tested, normalized so that the average intensity of R-alkanes in each pattern equals 1, show R-pores and R- $\pi$  reflections that are significantly higher than experiment and R-spots reflections that are slightly lower than experiment. R-double does not appear in any simulated patterns, and thus has no measurable intensity. In terms of the locations of the reflections, R-pores, R-alkanes and R-spots appear at  $q$  values that close to experiment, while R- $\pi$  appears at a significantly lower  $q$  value than experiment.

		Normalized Reflection Intensity			
Reflection	Experiment	Sandwiched	Parallel	Disordered	Disordered
		Displaced	Sandwiched	Parallel	Displaced
R-alkanes	1.0	1.0	1.0	1.0	1.0
R-pores	4.91	49.5	54.0	50.8	53.4
R-spots	1.2	1.2	1.2	1.1	1.1
R- $\pi$	2.8	44.0	7.7	8.4	10.1
R-double	0.9	—	—	—	—
Reflection Location ( $ \mathbf{q}  \text{ \AA}^{-1}$ )					
Reflection	Experiment	Sandwiched	Parallel	Disordered	Disordered
		Displaced	Sandwiched	Parallel	Displaced
R-alkanes	1.39	1.44	1.44	1.42	1.43
R-pores	0.176	0.170	0.170	0.173	0.172
R-spots	1.39	1.44	1.44	1.42	1.43
R- $\pi$	1.70	1.41	1.42	1.40	1.40
R-double	0.85	—	—	—	—

### 3.2.1 The location of R-alkanes

We normalized the experimental and simulated diffraction patterns so that the average intensity within R-alkanes is equal to 1 because we believe that R-alkanes is the experimental

feature most likely to be reproduced by our simulations. We reach this conclusion because alkane parameters in GAFF and AMBER forcefields generally reproduce data well.<sup>26,41</sup>

R-alkanes appears close to its expected location. In all cases, the maximum intensity of R-alkanes along the  $q_r$  axis at  $q_z=0$ , which we use to estimate its location, appears at a  $|\mathbf{q}|$  value that is, at most, 3.5% higher than experiment. The error in the simulated diffraction patterns is less than the error due binning in each frequency direction, so was not further investigated.

### 3.2.2 The location and intensity of R-pores

R-pores is about 10 times more intense than experiment in all simulated systems. Some or all of this discrepancy may be a consequence of our normalization of the experimental 2D SAXS pattern, since the common peak between it and the 2D WAXS patterns is partially obscured by the beamstop in the WAXS. If our simulations do indeed predict an intensity of R-pores that is too high, we hypothesize that this is primarily due to the relatively perfect infinite hexagonal array of pores in the simulated systems. In the real system, periodicity of the hexagonal array is disrupted by misalignment of the crystalline domains and the pore-to-pore distances fluctuate more over long time scales. The agreement in intensity in R-pores obtained here is sufficient for this study because this intensity is primarily controlled by longer-range organization that cannot be captured by simulation of only 4 pores and because we are only concerned with the structure of the individual pores themselves.

The location of the leading peak of R-pores is directly related to the average distance between pores. However, there is substantial uncertainty in the exact location relative to the bin size resulting from the Fourier space transformation. We can instead measure the average distance between columns with more precision in real space (See Section 2.5.2). We showed that we achieve experimentally consistent pore spacings in our simulations in Section 3.1.

### 3.2.3 The origin of R-spots

The intensity of R-spots is close to experiment when generated from any of our simulated systems. We measured its intensity as outlined in Section 2.5.3.

Previous literature has attributed the R-spots reflection in this particular WAXS dataset as the result of tilted alkane chains.<sup>16</sup> We measured the tilt angle of the alkane chains of the 280 K system by measuring the angle made by the vector extending from top to bottom of each tail with respect to the membrane plane. We found that it equilibrates to an average tilt angle of -2° (Fig. 8b), far from the 37° tilt angle previously used to explain R-spots. Even when we placed position restraints on the monomers in a tilted initial configuration, monomers quickly reduced their tilt relative to the *xy* plane to an angle statistically indistinguishable from zero (See Section S-14).

In order to more clearly identify the structural reasons for R-spots, we equilibrated an ordered basin sandwiched configuration at 280K to moderately increase the order and therefore intensity. Many force fields do not obtain the correct equilibrium structure at precisely the experimental temperature. Wang et al. highlighted the shortcoming of some of the most popular protein force field in predicting the temperature dependence of protein structural ensembles.<sup>42</sup> It is therefore possible that our membrane system, simulated at 300K, is understructured in the tail region compared to the experimental structure at 300K. We found that lowering the temperature indeed better resolved R-spots (Figure 8a), suggesting that our ‘effective’ temperature might indeed be too high, understabilizing structure.

The evidence from simulations strongly suggest that the source of the R-spots reflection is packing of the tails in a hexagonal array. First, we demonstrate R-spots comes primarily from the tails, by removing all non-tail atoms from the trajectory and simulating the XRD diffraction pattern with the remaining atoms, which preserves R-spots (Figure 8c). Next, we plotted the center of masses of the first four tail atoms of all tails (Figure 8d). We measured the angle between each COM and its nearest neighbor COMs with respect to the *xy* plane of the membrane. We see distinct peaks in the distribution of these angles located ca. -60°,

$0^\circ$ , and  $60^\circ$  which is consistent with a hexagonally packed configuration (Figure 8e). This ordering is primarily in the parts of the tail proximal to the heads, and dies off at the tail ends, where there is more space to fill causing them to pack nearly isotropically. See Section S-15 for a more detailed explanation of the calculation and packing distributions generated from different sections of the tails.

The peaks in the nearest neighbor angle distribution due to the hexagonal packing are consistent with the location of R-spots. The 2D Fourier transform of a simple hexagonal array constructed based on the peak angles in Figure 8e shows reflections in the same locations as R-spots, in addition to vertical stacking reflections along the  $q_z$  axis that would intersect with R- $\pi$  (Figure 8f).

### 3.2.4 The position, shape and intensity of R- $\pi$

The position, shape and intensity of R- $\pi$ , generated from simulations at 300 K have qualitative and quantitative differences from experiment. The reflections appear at lower  $q_z$  values, they are more intense, and the shape of its cross-sections, especially in the  $q_r$  direction are different relative to the experimental system. For comparison, see Figure 9 where we used cross-sections of the simulated XRD generated from the ordered parallel displaced configuration as an example. In this section, we explore the various contributions to these discrepancies, and use this information to speculate on what reasonable differences in the simulations could explain the discrepancies.

#### Distance and correlation between stacked monomer head groups

R- $\pi$  appears at a lower  $q_z$  value in our simulations versus experiment because monomers in the simulated system stack further apart than those in the experimental system (Table 2). We calculated  $z$ -direction pair distribution functions,  $g(z)$ , as described in Section 2.5.4. The resulting distributions are generally characterized by decaying oscillatory behavior where the average distance between peaks corresponds to the average distance between stacked

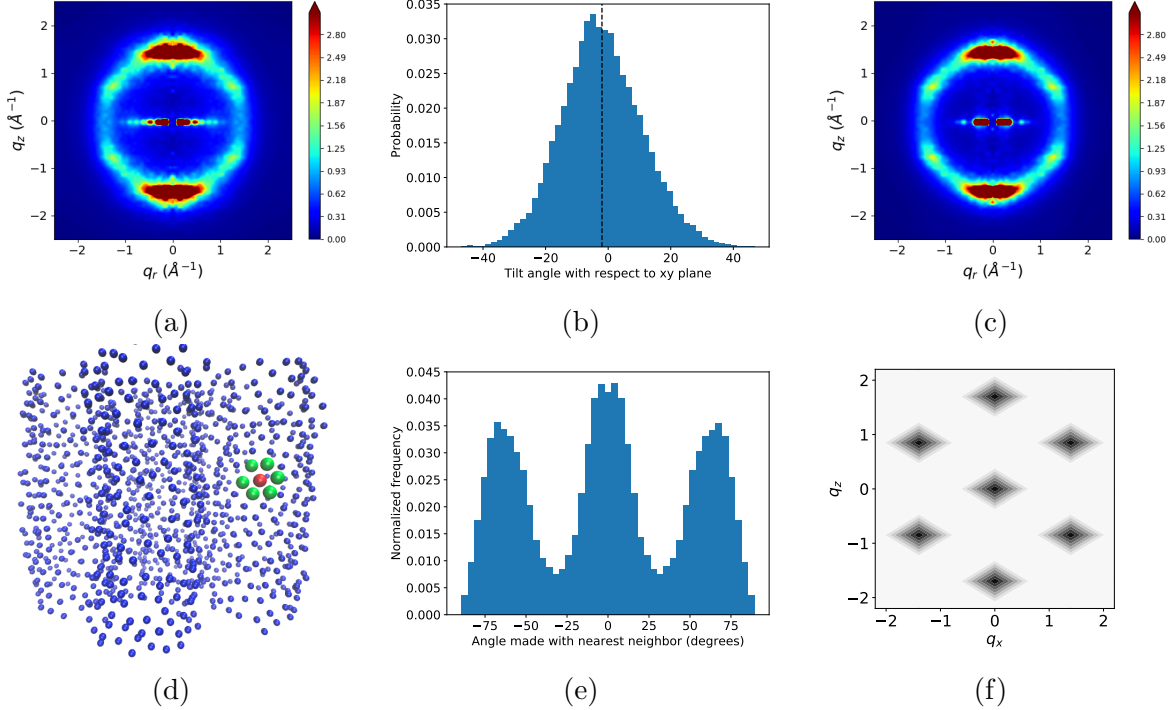


Figure 8: (a) R-spots increases in intensity when the temperature of the system is lowered to 280K. (b) We measured the average angle made between each monomer alkane tail and the membrane plane. The average tilt angle (dashed line) is near  $-2^\circ$  which is far from the  $37^\circ$  tilt angle previously used to explain R-spots. (c) To isolate the main cause of R-spots, we removed all atoms from the trajectory except for carbon atoms that constitute the tails. The simulated XRD pattern of the tails-only trajectory still shows R-spots. (d) Since the tails stay relatively flat, we plotted the center of mass of the first four carbon atoms of each tail originating from the head groups (for example, green colored centroids in the plot surround the red centroid in hexagonal fashion). Visually, the packing looks hexagonal. (e) We hypothesize that R-spots is the result of ordered tail packing. Defining the membrane plane to be  $0^\circ$ , we measured the angles between each center of mass and its nearest neighbor center of masses for the equilibrated sandwiched configuration simulated at 280K. Peaks appear in the distribution at  $-60^\circ$ ,  $0^\circ$  and  $60^\circ$ . (f) The Fourier transform of a hexagonally packed grid of points defined by the angles in (e) shows intensity at the same locations where we expect to see R-spots, as well as intensity along the  $q_z$  axis where R- $\pi$  would appear.

monomer head groups (Figure 10). We calculated this equilibrated vertical stacking distance,  $d_{equil}$ , between monomers using Equation 3. The distance between stacked monomers is greater than experiment by 0.5–0.9 Å across all cases, with disordered basins at the high part of that range and are on average 0.2 and 0.3 Å more distant. This behavior is not surprising since GAFF models atoms as point charges and does not appropriately model

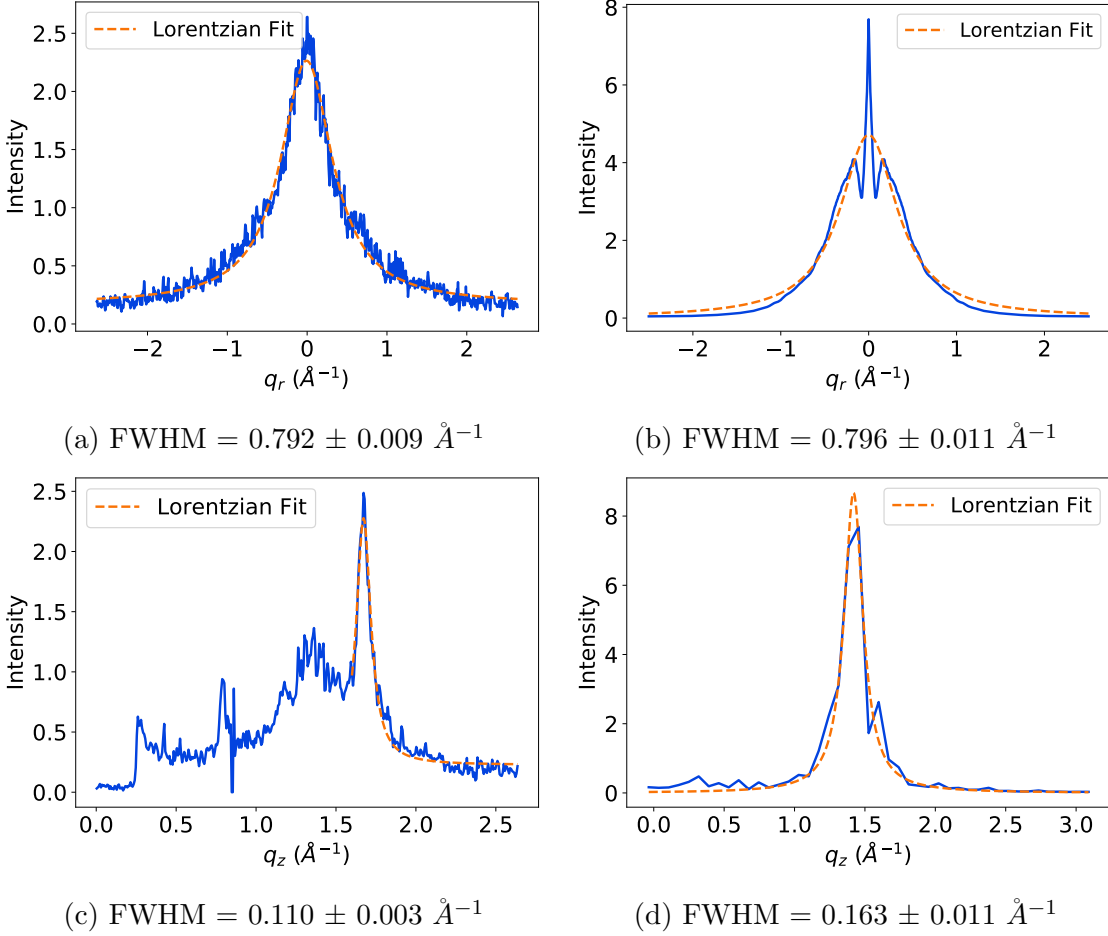


Figure 9: The maximum intensity of R- $\pi$  generated from simulations of the ordered parallel displaced configuration is 3 times larger than experiment. The  $q_r$  cross-section of R- $\pi$  ((a) and (b)) is qualitatively different between experiment (a) and simulation (b). We fit Lorentzian profiles to each peak and the FWHM (full width at half maximum) of the simulated pattern agrees with experiment within error. However the fit to the simulated data is affected by the three sharp peaks which appear near  $q_r = 0$ . The  $q_z$  cross-sections of R- $\pi$  ((c) and (d)) are qualitatively similar. Each fits a Lorentzian profile well, however the FWHM of the simulated cross-section (d) is 48% larger than the experimental cross-section. Additionally, the peak of the simulated  $q_z$  cross-section is located at a lower  $q_z$  value than experiment.

the aromatic  $\pi - \pi$  interactions, which would make it more energetically favorable for the monomers to stack closer together.<sup>26</sup> It is also possible that the tails prevent close stacking of monomer head groups and we do not achieve the timescales necessary for them to rearrange into a necessarily more tightly packed configuration. We equilibrated the system at 500 K then annealed it to 300 K in an attempt to coerce the tails into a more tightly packed configuration. Before annealing and in order to stabilize the hexagonal phase at 500 K, we placed harmonic restraints with force constants of  $1000 \text{ kJ mol}^{-1} \text{ nm}^{-2}$  between head group COMs within each column as well as between head group COMs in adjacent columns. We saw no improvement in packing distance over our 300 K models (See further discussion in section 3.4).

The system size, in the  $z$ -direction, does not significantly alter  $g(z)$ . In Figure 10, oscillations do not fully decay, so a taller system may be necessary to fully capture the correlation function. We therefore equilibrated a sandwiched system with twice as many monomers per column so that the system size doubled in the  $z$ -direction. The correlation length increases modestly from  $4.5 \pm 0.4$  to  $7.3 \pm 1.2 \text{ \AA}$ . However, visually, the correlation functions are nearly identical and oscillatory behavior persists throughout  $g(z)$  in both cases (See Figure S-3a).

The broadening of the  $q_z$  cross-section of R- $\pi$  is related to  $z$ -directional correlation between scatters within monomer columns. The correlation length varies as the inverse of the full width at half maximum (FWHM) of the  $q_z$  cross-section of R- $\pi$ . Using this technique, we calculated the correlation length of the experimental system to be  $9.0 \text{ \AA}$ . As scatterers become less correlated, we expect that R- $\pi$  will broaden.

The correlation lengths of vertically stacked scatterers in our atomistic simulations are in reasonable agreement with experiment. Since it is not feasible for us to simulate membranes with much taller columns in order to obtain increased  $q_z$  resolution of our simulated XRD patterns, and because the simulated peak shape is convoluted by the extremely intense maximum of R- $\pi$ , we measured correlation length by fitting Equation 2 to the peaks of  $g(z)$ . The correlation length of the parallel displaced, ordered basin system shows the closest

agreement with experiment (Table 2). We could not extract a reliable correlation length from the disordered parallel displaced configuration since the peaks do not show clear patterns that can easily be fit to an exponential decay. The correlation length of both sandwiched systems are relatively low because the height of the first peak of  $g(z)$  is so high.

Overall, we believe our simulations exhibit a realistic amount of distance correlation in the direction parallel to the pore axis between head groups within each column. The difference in the FWHM of the  $q_z$  cross-section of R- $\pi$  between experiment and simulation is less than one bin size (Figures 9c and 9d). The more significant difference between the two cross-sections is their maximum intensity which we study in more detail below.

**Table 2: The correlation length is larger for systems in the ordered basin. The equilibrated vertical stacking distance,  $d_{equil}$ , is also smaller.**

System	$d$ (Å)	$d_{equil}$ (Å)	Correlation Length (Å)
Sandwiched	3.7	$4.27 \pm 0.03$	$4.2 \pm 0.8$
Parallel Displaced	3.7	$4.33 \pm 0.04$	$14.5 \pm 1.3$
Sandwiched	5.0	$4.48 \pm 0.07$	$3.2 \pm 0.9$
Parallel Displaced	5.0	$4.60 \pm 0.08$	$< d_{equil}$
Experiment	–	3.70	$10 \pm 1$

### Shape and Intensity of the $q_r$ cross-section of R- $\pi$

In addition to the maximum intensity of R- $\pi$  being too high, the shape of its  $q_r$  cross-section in the simulated XRD is qualitatively different from experiment (Figures 9a and 9b). We attempted to fit a Lorentzian profile to the  $q_r$  cross-section and although the FWHM agrees with experiment within error, the fit is not optimal due to the three sharp peaks that appear near  $q_r = 0$ .

An exact quantitative comparison between the intensity and FWHM of the experimental and simulated cross-sections of R- $\pi$  is not feasible for several reasons. Experimental peaks broaden due to effects that we can not easily simulate such as finite size crystalline domains and instrumental resolution. In our simulated XRD patterns, the system size im-

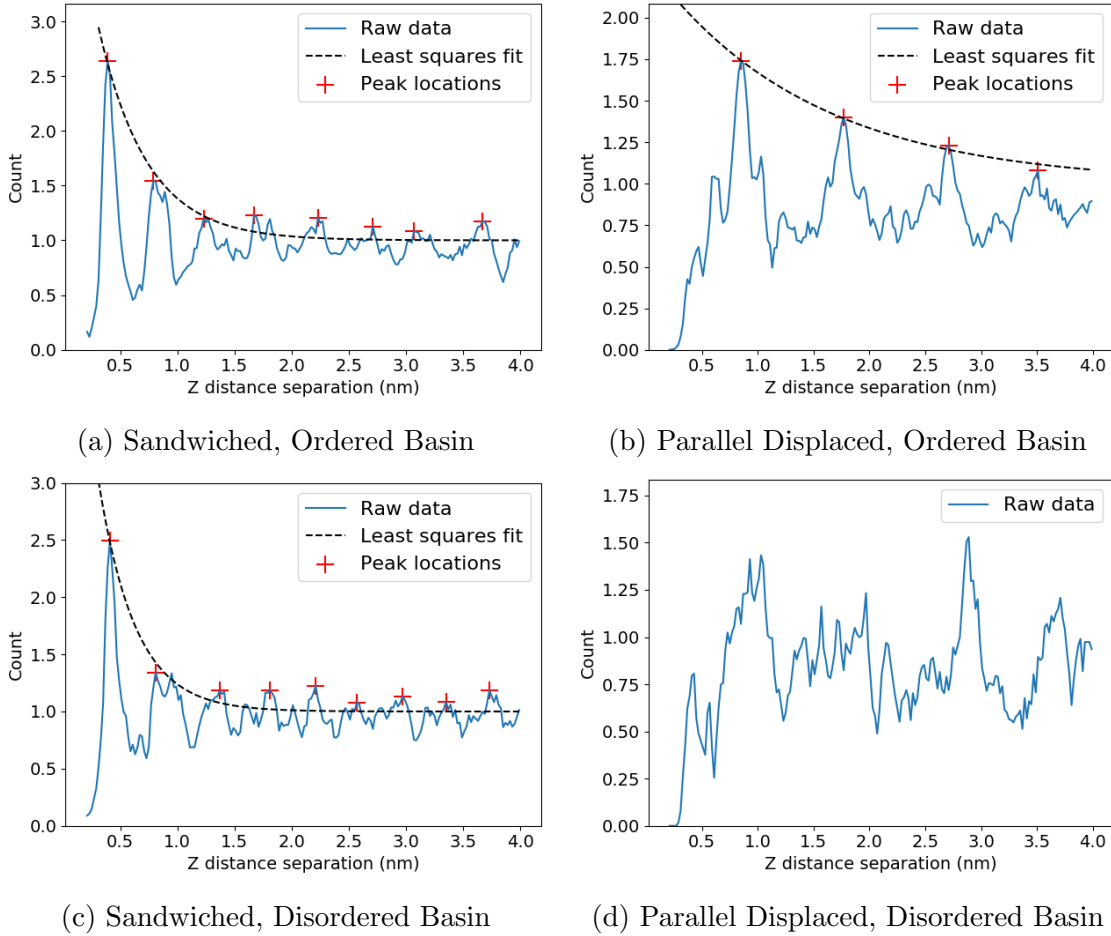


Figure 10: 1D correlation functions of the center of masses of aromatic head groups,  $g(z)$ , show decaying oscillatory behavior and have consistent correlation lengths with experiment. We calculated the correlation length by fitting a decaying exponential function (Equation 2) to the peaks of  $g(z)$ . The correlation length is longer for ordered basin systems (Table 2). We did not attempt to calculate the correlation length for (d) because there are no clear peaks. We assume that its correlation length is less than the vertical distance between monomers.

poses limitations on the resolution, which makes it difficult to reliably fit peaks. This is especially problematic when comparing the FWHM of the  $q_z$  cross-section of R- $\pi$ , where the experimental FWHM ( $0.11 \text{ \AA}^{-1}$ ) is similar to the bin size in the  $q_z$  direction (ca.  $0.07 \text{ \AA}^{-1}$ ). Additionally, we model each atom with a Gaussian sphere of electron density, which is a simplification. However, we can explore reasons for which differences in the simulation structure could change the peak shapes and intensities to be in better agreement with experiment.

We studied the shape and intensity of R- $\pi$  by setting up simplified systems where we

represent monomer head groups as point scatterers, as described in Section 2.6. The amount of quenched and thermal disorder present in the atomistic system, which we applied to the simplified systems, are given in Table 3. The quenched disorder, the deviation of monomers from idealized symmetric configurations, is several times greater than thermal disorder, the deviations of the monomers from their average positions during the production simulations. We hypothesize that, experimentally, the quenched disorder is the same as thermal disorder, but we cannot reach the necessary transition timescales to fully thermalize in these simulations.

**Table 3: Deviation of the positions of the center of mass of head groups from their average positions (thermal disorder) as well as their idealized positions (quenched disorder) to use as simulated disorder into our model system.**

System	Thermal Disorder			Quenched Disorder		
	$\sigma_x$ ( $\text{\AA}$ )	$\sigma_y$ (rad)	$\sigma_z$ ( $\text{\AA}$ )	$\sigma_z$ ( $\text{\AA}$ )	$\sigma_\theta$ (rad)	$\sigma_r$ ( $\text{\AA}$ )
Ordered Sandwiched	0.31	0.33	0.34	1.48	0.43	2.30
Ordered Parallel Displaced	0.51	0.52	0.30	1.45	0.43	2.28
Disordered Sandwiched	0.41	0.57	0.32	1.58	0.43	2.93
Disordered Parallel Displaced	0.39	0.31	0.33	1.65	0.43	2.63

Increasing thermal noise in the  $z$ -direction will reduce the intensity of R- $\pi$ , however the  $q_r$  profile remains unchanged. When we increase the thermal noise of the simplified parallel displaced system in the  $z$ -direction by 12% and 27%, we see a 3 and 15-fold decrease in the maximum intensity of R- $\pi$  respectively (Figure 11). Despite the decrease in intensity, the 3 cross-sections have the same shape (Figure 11b), whose sharp Bragg-like peaks are not consistent with experiment.

However, when we allow monomer columns to move independently in the  $z$ -direction, the intensity of R- $\pi$  drops and the  $q_r$  cross-section of the simulated diffraction patterns smooths out. We can demonstrate this by creating a simplified sandwiched configuration (simplified in the same way as described above), with varying amounts of statistical correlation between columns. In the low limit, the COM of columns are situated at the same  $z$ -coordinate. We allow increasing independence of columns by randomly shifting each column in the  $z$ -

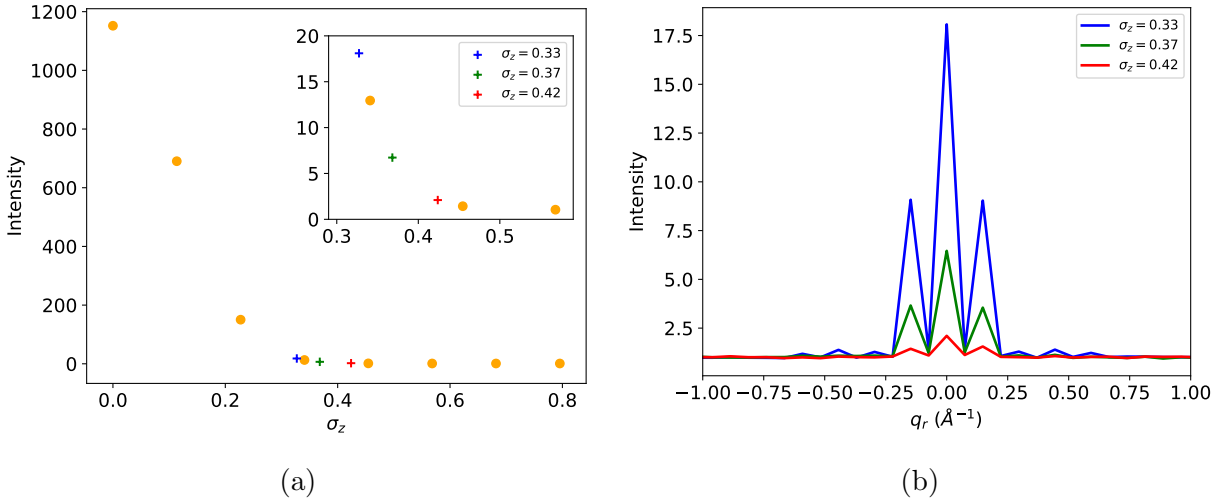


Figure 11: We can decrease the maximum intensity of R- $\pi$  by increasing thermal noise in the  $z$ -direction, however the  $q_r$  cross-section profile does not change. (a) The intensity of R- $\pi$  drops precipitously as we increase  $\sigma_z$ . We can decrease the intensity of R- $\pi$ , relative to the background intensity, relative to systems with simulation levels of disorder (blue) by a factor of 3 when we increase  $\sigma_z$  by 12% (green) and by a factor of 15 when we increase  $\sigma_z$  by 27%. (b) Although the maximum intensity of R- $\pi$  decreases with increasing  $\sigma_z$ , the peak shape remains the same.

direction according to a uniform distribution bounded by  $(0, f \times d_{equil})$  where  $f$  ranges between 0 and 1. We limit this discussion to the sandwiched configuration since it is not feasible for columns in the parallel displaced configuration, as we have set them up, to move past each other. When  $f = 1$ , the columns move independently and the  $q_r$  cross-section smooths out completely (Figure 12). Any amount of dependence results in some presence of independent sharp peaks, though significantly attenuated at  $f$  nearer 1. The intensity of R- $\pi$  also decreases with increasing column independence. We see an 8-fold decrease in the intensity of R- $\pi$  when  $f = 1$  versus when  $f = 0$  for our simplified model systems.

It therefore seems likely that the discrepancy between the intensity of R- $\pi$  generated from our simulations versus experiment is primarily due to highly correlated columns in our initial configurations, likely due to the highly symmetric starting configuration. If the columns were uncorrelated,  $g(z)$  of the ordered sandwiched system would very closely resemble Figure 10a when we average all  $z$ -slices of the 3D correlation function. When we include all  $z$ -slices in  $g(z)$  for our system, rather than restricting it to those  $z$ -slices within 2.1 Å of the center

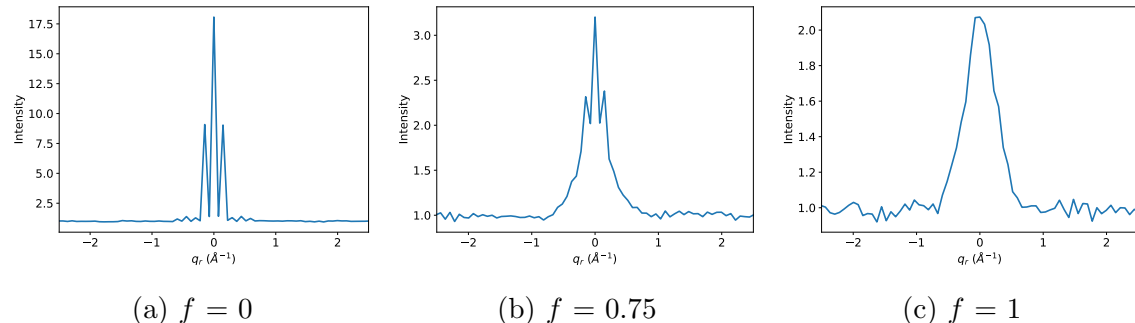


Figure 12: As we increase column independence using the  $f$  parameter, the intensity of R- $\pi$  decreases and the  $q_r$  cross-section of the simulated diffraction pattern becomes more smooth. (a) When we place all columns at the same reference  $z$  coordinate,  $f = 0$ , the intensity of R- $\pi$  is 18.3 and is characterized by sharp Bragg-like peaks. (b) When columns have a moderate amount of independence,  $f = 0.75$ , the intensity of R- $\pi$  decreases 5-fold to 3.7. The edges of the peak are beginning to smooth out, but sharp peaks still exist. (c) When columns are completely independent,  $f = 1$ , the intensity of R- $\pi$  decreases 8-fold to 2.3 and the cross-section is relatively smooth.

of the correlation function (Section 2.5.4), the function shows oscillatory behavior and the correlation length nearly triples to  $12.4 \pm 0.7$  Å. (Figure 13). Since all columns in our initial configuration are started at the same  $z$ -coordinate,  $g(z)$  on average exhibits correlation of head groups with other head groups within the same column, with head groups in other columns within the same pore, and with head groups in different pores.

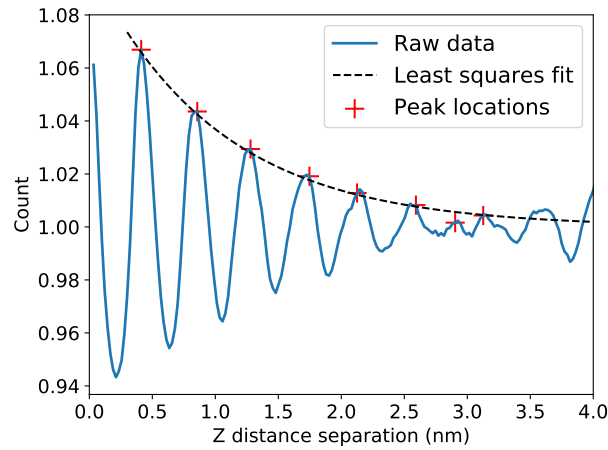


Figure 13: When we average all  $z$ -slices of the 3D correlation function, the correlation length of the ordered sandwich configuration nearly triples.

Increasing thermal noise in the  $xy$  plane causes the FWHM of the  $q_r$  cross-section of R- $\pi$

to, somewhat counterintuitively, decrease. Using a system with uncorrelated columns, we modified the disorder in both the  $r$  and  $\theta$  directions by multiplying their values by a factor of 0.5 and 2 (Figure 14). When we cut the noise in half, the FWHM increases by 88%. When we double the noise, the FWHM decreases by 51%. As we have fit the data in Figure 9b, the FWHM of R- $\pi$  agrees well with experiment, meaning the quenched configuration contains about the right amount of disorder on the  $xy$  plane. However, the relatively low quality of the fit implies that the FWHM may be incorrect, and that the radial ordering of the head groups may benefit from further optimization.

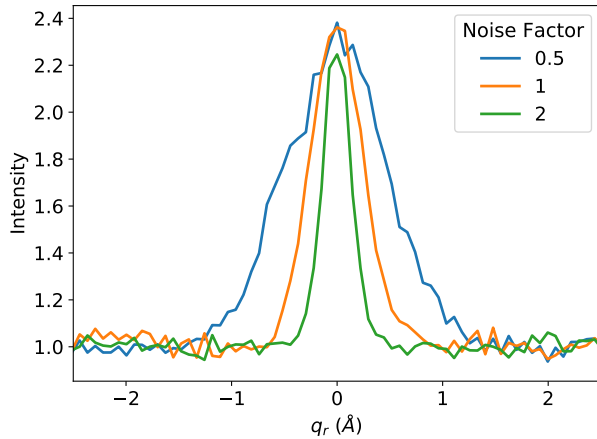


Figure 14: Increasing the amount of disorder in the  $xy$  plane decreases the FWHM of the  $q_y$  cross-section of R- $\pi$ . When we cut the amount of  $r$  and  $\theta$  disorder in half (Noise factor = 0.5), the FWHM increases by 88%. When we double the disorder (Noise factor = 2), the FWHM decreases by 51%.

### Quenched disorder in ensembles of configurations

Since the dynamics of this system are slow, and consequently most of our analysis has been focused on a set of quenched configurations with some structural characteristics that do not vary significantly with time, we attempted to learn more about their time-averaged structures by studying ensembles of shorter simulations started from more independent initial configurations. We created ensembles of 40 simulations in both the parallel displaced and sandwiched configurations. We used the same equilibration scheme as above (see sec-

tion 2.4). However, we built the initial configurations with randomly displaced columns in the  $z$ -direction and looked at the results after 5 ns of unrestrained simulation, which should capture any quenched disorder built in from the initial configurations. We then simulated XRD patterns from the 40 trajectories, concatenated together. The  $q_r$  cross-sections of R- $\pi$  generated from the two concatenated trajectories are shown in Figure 15. Qualitatively, the cross-sections of are nearly smooth, with only small spikes near  $q_r=0$ . These data suggest that the average intensity of R- $\pi$  in the ensemble of sandwiched systems is about 3× higher than that in the ensemble of parallel displaced configurations. Compared to our long simulations, the intensity of R- $\pi$  generated from ensembles of short simulations, decreases by a factor of 3 and by a factor of 2 for the sandwiched and parallel displaced configurations respectively. Overall, the intensity of R- $\pi$  generated from the parallel displaced ensemble shows the best agreement with experiment so far. For simplicity, we will limit the following discussion to the parallel displaced configuration. Equivalent data is available for the sandwiched configuration in the supporting information.

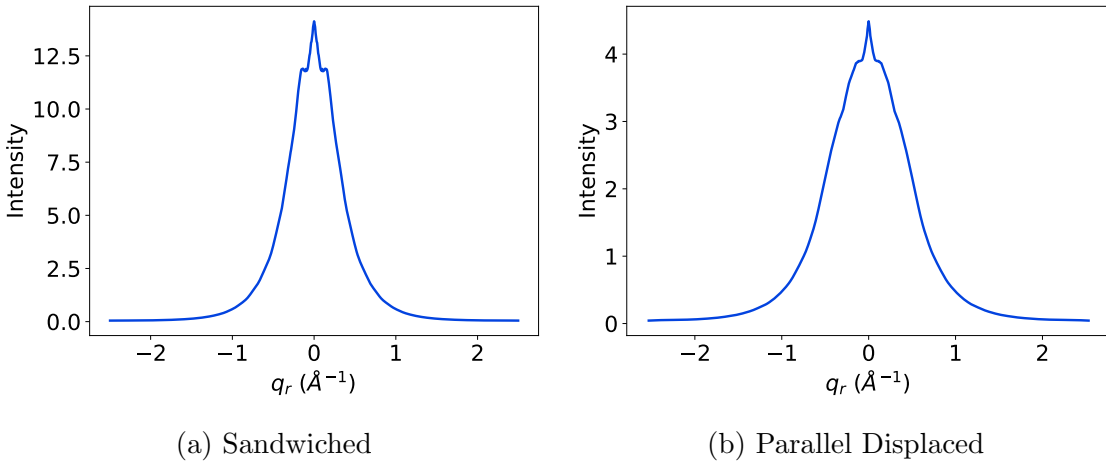
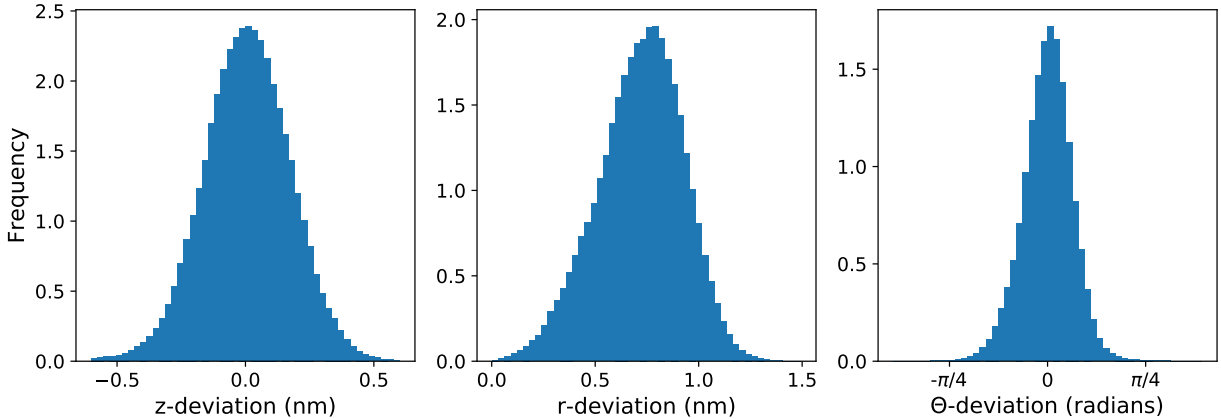


Figure 15: The  $q_r$  section of R- $\pi$  is much smoother when we generate simulated XRD patterns from an ensemble of 40 independent simulations, suggesting that much of the extra initial intensity may be due to the starting conditions. The maximum intensity of R- $\pi$  is 3× higher in the sandwiched configuration (a) than in the parallel displaced configuration (b).

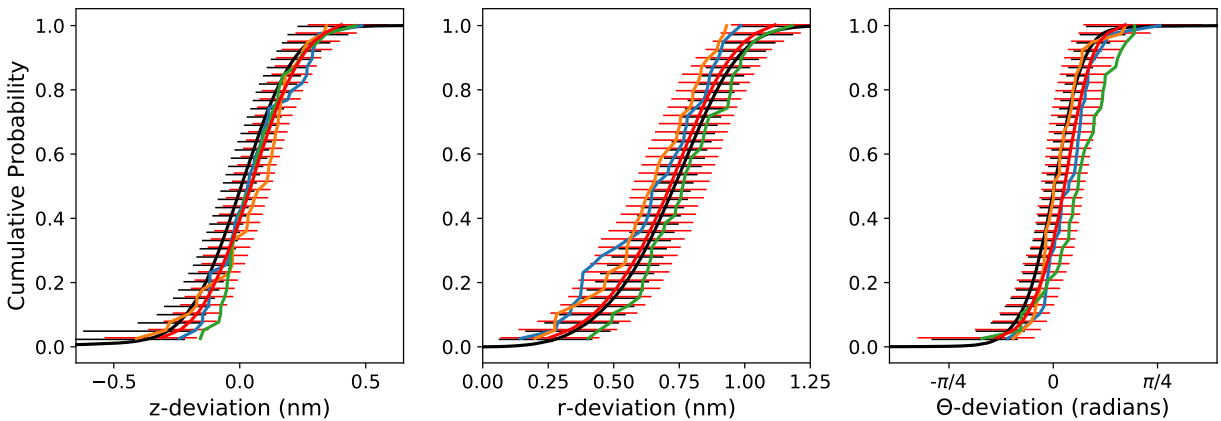
These short independent simulations exhibit similar amounts of quenched disorder. We pooled the deviations of each head group COM from idealized positions from all independent

simulations in order to create the distributions shown in Figure 16a (see section 2.6). The distributions appear symmetric meaning that there is an equal chance for a head group to displace in the positive or negative  $z$ ,  $r$  or  $\theta$ -direction. We verified that this is the case for individual COMs. If we consider the COM of a given head group, we expect that the distribution of its deviations from its idealized position among all the independent simulations should be symmetric about its idealized position. We can calculate the empirical cumulative distribution function (ECDF) of these distributions of deviations. The ECDFs of 3 randomly selected COMs are shown in Figure 16b to guide the eye (colored lines). The average of all COM ECDFs is represented by the red line with the 95 % confidence interval represented by the red error bars. We also calculated the ECDF from the full distributions in Figure 16a (black line with error bars). We generated error bars that represent the 95% confidence intervals by performing 1000 trials where we randomly sampled 40 values (the same as the number of independent simulations) from the distributions in Figure 16a, then measured the deviation between the sampled ECDF and the full ECDF. These error bars are generally smaller than those generated from the 400 COM ECDFs, as there is a wider distribution of mean COM deviations than the mean deviations from distributions sampled from the full distribution. The similarity between entirely independently sampled ECDFs and the ECDFs from individual independent simulations supports the hypothesis that each quenched configuration is random and mostly independent.

The systems that we simulated for 400 ns and then used for most of our analysis are representative of the long term simulation behavior of any system chosen from the ensemble. The distributions of standard deviations generated from each of the ensemble trajectories (Figures 17a and 17b) are fairly tight with  $(\sigma_{\sigma_z}, \sigma_{\sigma_r}, \sigma_{\sigma_\theta}) = (0.011 \text{ nm}, 0.007 \text{ nm}, 0.022 \text{ radians})$ . We analyzed the first 5 ns of the 400 ns ordered parallel displaced configuration and observed the same amount of disorder (based on the  $\sigma$  values in Figure 17a) with indistinguishable mean values. Additionally, we calculated the radial density of monomer components as a function of their distance from the pore centers (Figure 17c). All simulations



(a) Distributions of deviations from ideal positions generated with data from all independent simulations



(b) Empirical cumulative distribution functions generated from (a) and from simulation ensembles.

Figure 16: (a) The distributions of the head group COM deviations from their idealized positions generated using pooled data from all frames of each independent configuration are symmetric, implying that there is equal probability for a head group to displace in the positive or negative  $z$ ,  $r$  or  $\theta$ -direction. (b) The COM position of a given head group is displaced randomly upon quenching. The ECDF generated from the pooled distributions (black) in (a) agree with the means of the ECDFs generated from each COM (red). The red error bars are larger than the black error bars since there is a wider distribution of mean COM deviations than the mean deviations of distributions sampled from the full distribution.

have similar profiles. The distribution of sodium ions near the pore center is relatively noisy since the sodium ions have much more translational freedom than the head groups.

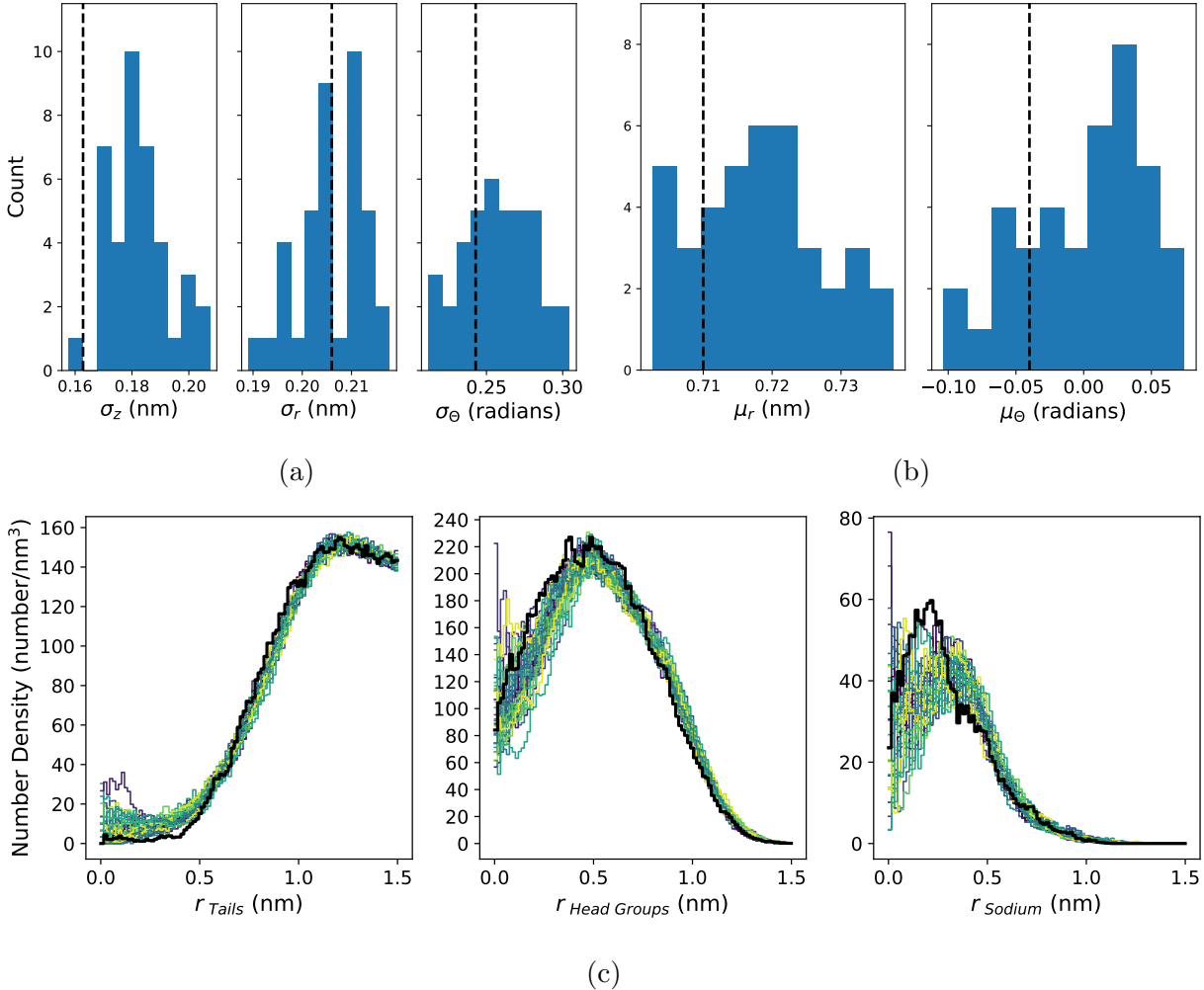


Figure 17: (a) The standard deviation of the distribution of quenched disorder from the first 5 ns of the main ordered parallel displaced system studied in this paper (black dashed line) is in agreement with the distribution of quenched disorder standard deviations calculated from the ensemble of simulations (histogram). (b) The mean values of  $r$  and  $\theta$  from the first 5 ns of the main system trajectory (black dashed line) is in agreement with the distribution of mean values calculated from each simulation in the ensemble (histogram). The mean values of  $z$  are necessarily 0 so they are not plotted. (c) The radial densities of tail atoms, head group atoms and sodium atoms calculated from the first 5 ns of the main system simulation trajectory (black lines) and from the ensemble of trajectories (all other lines) look qualitatively similar.

### The implications of the new-found understanding of R- $\pi$

We can explain the discrepancies between R- $\pi$  seen experimentally and in simulation using what we have shown in this section. The stacking distance between monomer head groups is too large, likely due to failures of the force field to appropriately model  $\pi-\pi$  interactions. The

intensity of the simulated R- $\pi$  is too high, which may be a consequence of too much short-range ordering in the  $z$ -direction in addition to high degrees of correlation between columns. Finally, the  $q_r$  cross-section of R- $\pi$  is not smooth, which is also likely a consequence of columns that are too highly correlated. If we limit ourselves to standard simulation techniques, it is necessary to average data generated from ensembles of independent simulation trajectories in order to begin converging on time-averaged descriptions of the system's molecular structure.

A secondary conclusion drawn from the evidence in this section is that the architecture of each column is likely in between our sandwiched and parallel displaced configurations. The parallel displaced configuration that we have simulated in this paper is an exaggerated manifestation of the parallel displaced  $\pi - \pi$  stacking mode. Not only is the intensity of R- $\pi$  calculated from the ensemble of parallel displaced simulations in close agreement with experiment, but the experimental WAXS pattern shows faint off-axis features at the same  $q_r$  value as R-double which are only present in simulated patterns generated from parallel displaced configurations. The monomers may prefer to be parallel displaced, but their displacement is likely only slightly shifted, on the  $xy$  plane, from the center of mass of their vertically adjacent neighbors (See Figure S-9). In this way, columns can more easily act independently while maintaining some features of parallel displaced structure.

### 3.2.5 Origin of R-double

R-double does not appear in any of the simulated diffraction patterns generated using the systems simulated up to this point. Here we hypothesize a few initial configurations which may lead to the appearance of R-double and show that we cannot achieve a long-term stable system that exhibits R-double without the inclusion of small amounts of water in the pores.

The appearance of R-double implies a vertical modulation in electron density every 7.4 Å. We are not able to achieve such modulation using our simple initial configurations. Although the position of monomers in parallel displaced configurations alternate every other layer, such a configuration will not produce R-double, but only off-axis reflections at the same  $q_z$  value.<sup>43</sup>

There is not a unique solution that describes the origin of R-double. Extracting the exact relationship between a diffraction pattern and its real space configuration is well-known as the phase problem.<sup>44</sup> We have proposed configurations that result in the appearance of R-double below, and we can speculate which makes the most physical sense. It appears that we cannot achieve a long-term stable system that exhibits R-double without the inclusion of small amounts of water in the pores.

One way to produce R-double is if our initial configuration contains alternating parallel and anti-parallel carboxylate groups relative to the plane of the monomer's phenyl ring. It is difficult to physically justify this system. Systems built this way are only stable if position restraints are placed on all head group heavy atoms. Carboxylate groups quickly revert to the parallel position as restraints are released. There is an appreciable energy barrier that prevents rotation of carboxylate groups attached to phenyl rings since the group extends the system's  $\pi$  conjugation<sup>45</sup> (See Figure S-23), which is significant even considering possible overestimates of the barrier height in the classical force field.

Another way to produce R-double is if we rotate monomers with respect to vertically adjacent monomers. In this configuration, monomers are rotated so that the vector created by the bond extending from the carboxylate carbon to the phenyl ring is oriented  $\pm 15^\circ$  with respect to the vector extending from the head group COM to the pore center (Figure 18a). Every other monomer layer is rotated  $+15^\circ$  and those in between are rotated  $-15^\circ$ . This configuration allows monomer tails to sit between adjacent monomer tails which may be the most favorable way for them to pack. This configuration is only stable for a few nanoseconds but R-double quickly fades.

We can also produce R-double if monomers are not uniformly spaced in the  $z$ -direction, but instead form pairs that stack less than 3.7 Å apart, with COMs that are spaced 7.4 Å from neighboring pairs of monomers (Figure 18b). Our force field causes our system to tend towards uniformly spaced layers. Simulations of unevenly spaced systems are only stable if position restraints are applied to heavy atoms of the phenyl rings. Additionally,

there is little evidence from QM studies of stacked  $\pi - \pi$  systems that such uneven stacking could be energetically stable.<sup>46</sup>

The addition of water to the system promotes the appearance of R-double, providing an answer to Question 3. We added water to the parallel displaced and sandwiched configurations in the ordered basin and equilibrated them according to the wet equilibration procedure. There is no experimental measurement of water concentration in these membranes so we tested a range of water concentrations from 1% to 5%. R-double appears transiently in the simulated XRD pattern of the parallel displaced configuration with 1 wt% water (Figure 18c). It is not initially present, but appears after 200 ns of simulation time. After 450 ns, it disappears again. Simulated XRD patterns of all other solvated systems tested are shown in Figure S-24, however R-double is not present.

R-double appears in the solvated system due to the structuring of the head groups. To demonstrate this, we removed the head groups from the trajectory used to produce Figure 18c in order to produce that shown in Figure 19a. R-double does not appear without the presence of the head groups. Water molecules must therefore play a role in the structuring of the head groups since R-double does not appear in any dry simulations.

When two vertically stacked monomer head groups hydrogen bond with a shared water molecule, the monomers are drawn closer together (as illustrated in Figure 19b), which creates an asymmetry that allows R-double to appear. If a monomer head group shares a hydrogen bonded water molecule with a head group above itself, it will be less likely to share a water molecule with a head group below it due to geometric constraints. The monomer head group below can just as easily share a water molecule with a head group below itself. In this scenario, the COMs of each pair are 2 times the  $\pi$ -stacking distance apart which would lead to R-double (much like the configuration in Figure 18b). There are a modest number of occurrences of this scenario, which we quantify in further detail in the Supporting Information, Section S-18.

Of all the configurations tested, it is most likely that R-double is induced by water

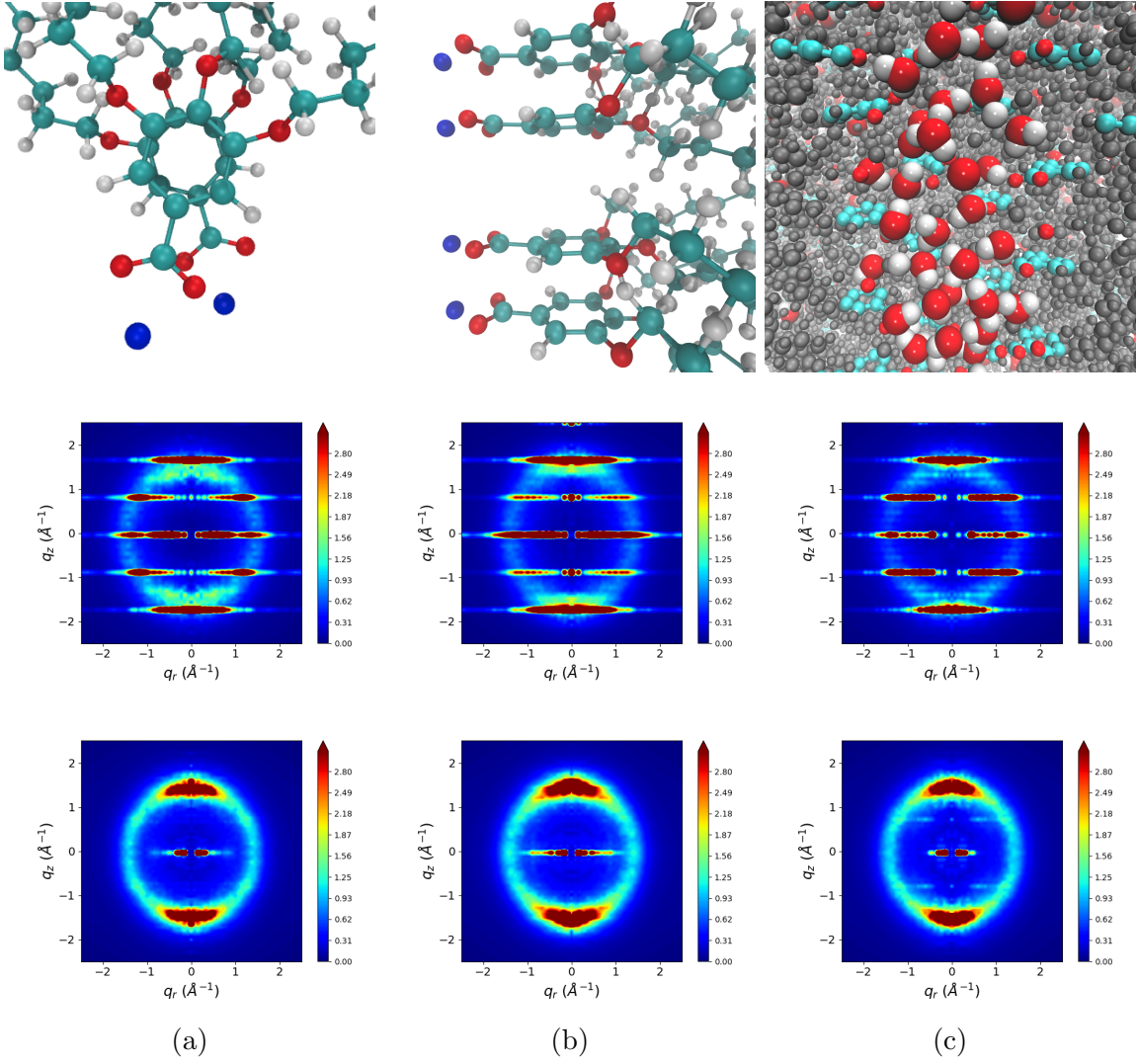


Figure 18: (a) When monomer head groups are rotated with respect to vertically adjacent monomers (top), R-double is visible while the heavy atoms of the head groups are held in place with position restraints (middle). Again, R-double fades once the position restraints are released. (b) When monomers are non-uniformly spaced (top), R-double appears if all heavy atoms of the head groups are held in place with position restraints (middle). R-double quickly fades once the position restraints are released (bottom). (c) When we add 1 wt% water to the parallel displaced configuration in the ordered basin (top) R-double is not initially present during the restrained portion of equilibration (middle). After 200 ns of equilibration, R-double becomes visible and persists for another 200 ns (bottom).

molecules as described above since it is the only mechanism that can be observed without position restraints. The extent of the hydrogen bonding network that forms is largely determined by the accuracy of the forcefield. It is possible that a more realistic force field would make the effect stronger or weaker. If this is truly the mechanism, it implies that the system

studied by Feng et al.<sup>16,19</sup> was not truly a thermotropic Col<sub>h</sub> phase. Rather, they were very low water content H<sub>II</sub> phases unintentionally created due to the neat monomers' hydroscopicity. Anecdotal evidence from other researchers suggests that membranes are less likely to assemble under completely dry conditions, supporting the idea that the “dry” structures do absorb some water. This detail may therefore be important for reproducing the results of Feng et al.

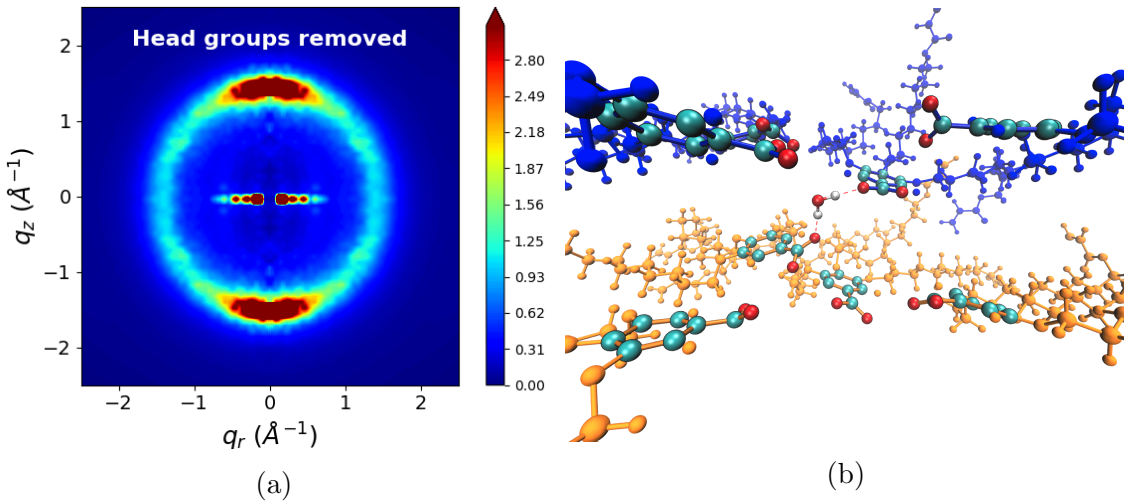


Figure 19: (a) The structure of the head groups is responsible for the appearance of R-double. When we remove head groups from the trajectory, the simulated diffraction pattern no longer shows R-double. (b) Monomer head groups above or below each other that hydrogen bond with a shared water molecule are drawn closer together in the  $z$ -direction. Blue monomers were stacked above orange monomers in the initial configuration.

### 3.3 Atomistic structure of pore columns

We are most interested in the structure and composition of the pores since we would like to study transport mechanisms within them. We have shown that the tails possess a certain degree of order which is necessary in order to create the complex WAXS pattern shown experimentally, but they will not be involved in a separation process. We aim to further understand the pore architecture, in order to address Question 4, and observe the differences, if any, between the different equilibrated configurations studied so far.

In general, the composition of each region, particularly within our definition of the pore

region, is similar between all systems. This suggests that the details of transport may be relatively independent of the structural differences between different possible structures studied here.

We plotted the number densities of heavy atoms in the head group, carbon atoms in the tail region and all sodium ions (Figure 20). For the head group region, we used heavy atoms making up the aromatic rings and carboxylate groups. For the tail region we used carbon atoms of the monomer tails (See Figure S-12 for a diagram). We averaged the histograms over at least 50 ns of equilibrated trajectory.

There is a gradient in pore composition transitioning radially from the hydrophilic to the hydrophobic region, rather than an abrupt division. Based on size-exclusion experiments, we define the pore radius to be 0.6 nm.<sup>11</sup> The system does not confine sodium ions and head groups to just within this experimentally-defined pore region. For dry systems, 19% of sodium ions exist outside the pore region (except sandwiched, ordered basin, where 16% are outside the pore). Additionally, we see that in all cases, about 3% of the plotted tail density is located within the pore region (except ordered sandwiched, where 1.5% are within the pore region). For the solvated system, the results are similar, however the head group density is shifted slightly radially outward, due to swelling of the pore by water.

The space in the pore region is filled with a mixture of sodium ions and head groups. The distributions appear somewhat different near  $r=0$ , but noise is higher since there is significantly less sampling as  $r$  approaches 0. Regardless, all systems, including the solvated system, have a significant number of head groups and sodium ions occupying the pore center. This observation highlights that the pore region is dense, not hollow, and may impede transport of solvent and solutes when compared to the previous idealized picture of a hollow tube conducive to transport.

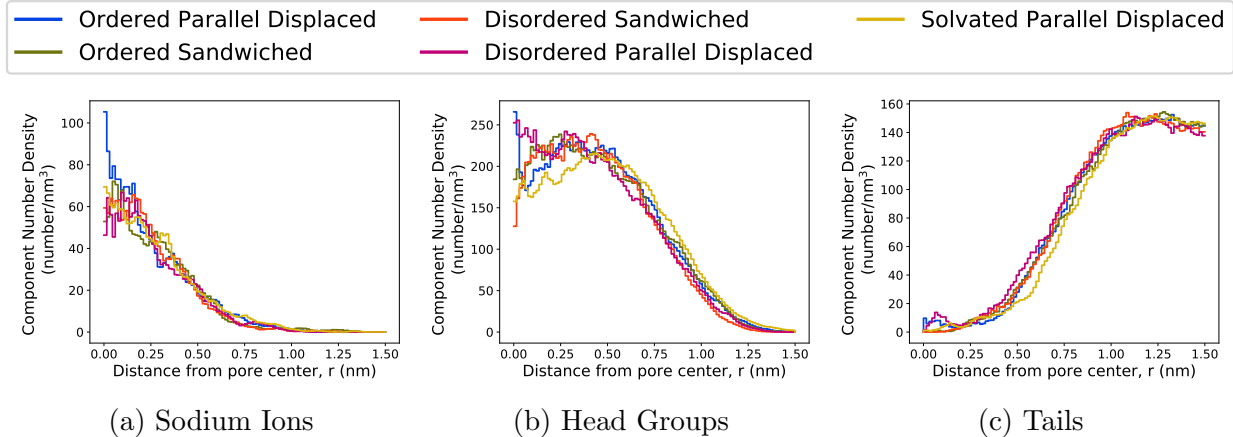


Figure 20: In all cases, the component radial distribution functions are similar. They exhibit a composition gradient transitioning from the hydrophilic to the hydrophobic regions. The biggest differences are at  $r=0$  where noise is higher due to decreased sampling. The center of the pore is not hollow, but contains sodium ions and head groups, even when the system is solvated. This architecture may impede transport in the real system in a chemically-dependent manner. The solvated system has a lower density of head groups near the pore center which is likely due to the swelling that is necessary in order to fit water molecules in the pore region.

### 3.4 Slow dynamics

We observe slow dynamics in our system. Typical diffusion constants for columnar liquid crystals have been reported to be between  $10^{-11} \text{ m}^2/\text{s}$ <sup>47</sup> and  $10^{-14} \text{ m}^2/\text{s}$ .<sup>48</sup> We measured the diffusion constants of monomers in each of the systems we studied (See Table S-3) and learned that they are all on the order of  $10^{-14} \text{ m}^2/\text{s}$ . However, since on this timescale, no monomers move a full ‘level’ above or below, this may be an overestimate. This slow speed is not entirely surprising considering how densely the monomers are packed as implied by diffraction experiments. The entangled tails likely restrict both vertical and lateral movement.

Consequently, there is not enough movement on the timescales we simulated for the system to consistently reach a definitive equilibrium structure. In all cases our monomers equilibrate to a stacking distance that is too large compared to experiment. While this may be in large part due to the force field’s inability to model aromatic interactions, it is also possible that the monomer tails do have enough time to pack as tightly as they could. More

densely packed tails could allow the monomers to stack closer together.

We quantified the movement of the tails during our simulations by calculating the auto-correlation function of the dihedral angle formed around the bond between the head groups and the ether oxygens which attach the tails to the head group (See Figure S-26). We exclude the dihedral from the middle tail since it is fundamentally different than the two symmetric outside tails. We limited these studies to the sandwiched configuration for simplicity.

The ether dihedrals become decorrelated on a reasonable timescale when we raise the system temperature. At 300 K (Figure 21a), the autocorrelation function does not cross the *x*-axis until  $\sim$ 105 ns meaning that tails fully rotate on average about 4 times over the course of the 400 ns that we studied. Additionally, the correlation function plateau's near a value of -0.2 which indicates that the tails are starting in an unfavorable configuration. We implemented distance restraints between the centers of mass of monomer head groups to preserve the hexagonal phase, then raised the temperature of the equilibrated 300 K ordered basin sandwiched system to 500 K. We witnessed decorrelation of the ether dihedrals after  $\sim$ 11 ns with a plateau at 0, (Figure 21b) indicating a complete loss of memory. We annealed the resultant configuration back down to 300 K over 200 ns to see if the increased rotational freedom might allow the system to relax into to a more tightly packed configuration.

Decorrelating the ether dihedrals at high temperature, followed by thermal annealing does not improve packing in our model. In the ideal case, if all monomers stacked 3.7 Å apart, the *z*-dimension of our unit cell should be 7.4 nm. In the ordered basin, sandwiched system studied in this paper, the *z*-dimension of the unit cell equilibrated to 8.87 nm, which is roughly consistent with the stacking distance reported in Table 2. After 200 ns of annealing from 500K to 300K, the *z*-dimension of the unit cell was 9.22 nm. We repeated the annealing procedure over the course of 400 ns and the final *z*-dimension of the unit cell was 9.20 nm. Much longer annealing simulations may get the system to the correct density, but such simulations are beyond the scope of the current study.

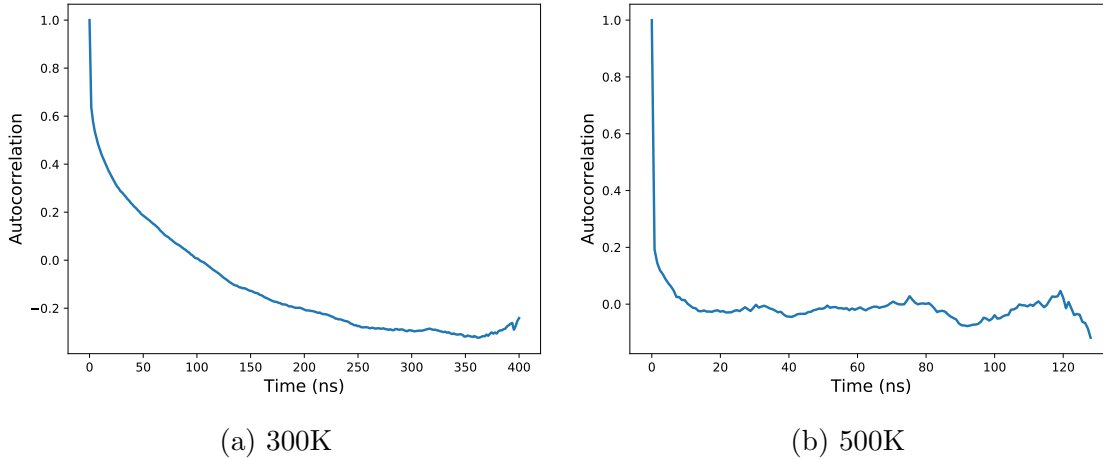


Figure 21: The outer tail ether dihedrals become decorrelated on a reasonable timescale when we raise the system temperature. (a) The dihedrals do not become decorrelated for ca. 100 ns when the system is equilibrated at 300 K. (b) The ether dihedrals become decorrelated after 11 ns when the temperature of the system is increased to 500 K.

### 3.5 Ionic Conductivity Measurements

We calculated the ionic conductivity of the parallel displaced configuration in the ordered basin with 1 wt% water since we believe its structure is the closest match to experiment. Our model estimates the ionic conductivity to be  $(5.92 \pm 0.05) \times 10^{-5}$  S/m, about 5 times higher than the experimental value of  $(1.3 \pm 0.1) \times 10^{-5}$  S/m. We verified the value calculated by the Nernst-Einstein relationship using the collective diffusion model<sup>49</sup> (See section S-15). The values calculated by the collective diffusion model agree with Nernst-Einstein values within error, however there is a much higher uncertainty that would require much longer simulations to lower.

The calculated value of ionic conductivity is 5 times higher than experiment because we simulated infinitely long, aligned pores. The ionic conductivity measurement to which we are comparing was done with an 80  $\mu\text{m}$  thick film, nearly 10,000 times thicker than our simulated system. The thick film is likely imperfectly aligned and has defects leading to non-contiguous pores. It has been shown that there is a large dependence of ionic conductivity on the alignment of the pores. The ionic conductivity of an isotropically aligned film is ca. 85 times lower than that of the nearly aligned film to which we are comparing.<sup>16</sup> We

hypothesize that a thin, perfectly aligned film would have a value of ionic conductivity in closer agreement with our model.

### 3.6 Effect of Cross-linking

Experimentally, membranes are cross-linked for mechanical stability before use. We applied our cross-linking algorithm to equilibrated sandwiched and parallel displaced configurations in the ordered pore basin. We allowed the cross-linking algorithm to propagate until greater than 90% of vinyl groups were either involved in a cross-linking reaction or were terminated (see section S-11 for further details of the cross-linking algorithm). We allowed the cross-linked configurations to simulate for 100 ns further in the NPT ensemble.

There are only minor changes to the physical characteristics of these systems when they are cross-linked (See Figure 22). The ionic conductivity of the sandwiched configuration decreases while that of the parallel displaced configuration stays the same. The pore spacing decreases in both systems by 0.07 nm. The vertical monomer stacking distance increases in the sandwiched configuration and decreases in the parallel displaced configuration, however the values of cross-linked configurations fall within uncertainty of their un-cross-linked counterparts. The correlation length decreases in both systems, but is most pronounced in the parallel displaced system.

## 4 Conclusions

We have used detailed molecular modeling of the Col<sub>h</sub> phase formed by Na-GA3C11 in order to study its nanoscopic structure. While there have been efforts to model formation of various liquid crystalline phases with molecular dynamics, to our knowledge there have been no studies which attempt to examine their structure with the same level of detail presented here.

We observed a number of metastable configurations, stable for hundreds of nanoseconds,

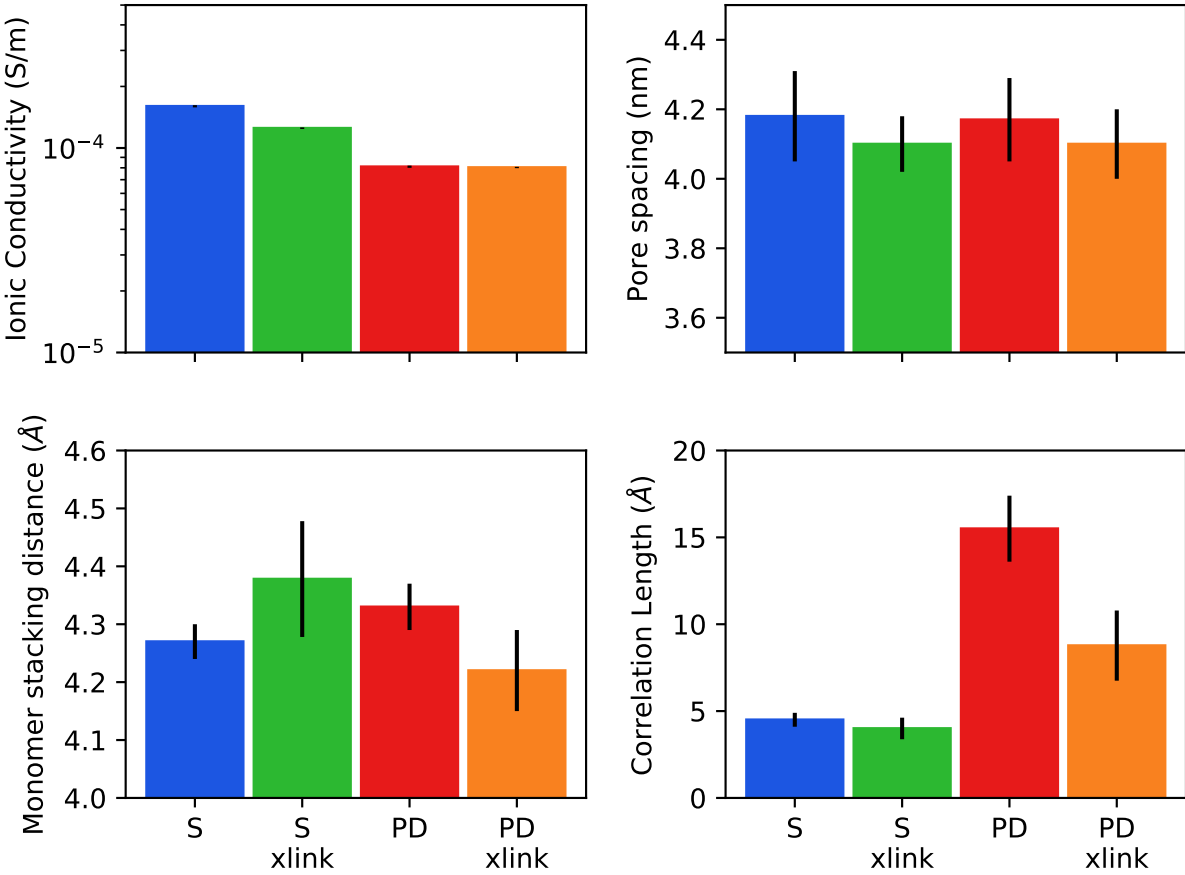


Figure 22: There are minor differences between the physical properties of a crosslinked (xlink) system versus an uncrosslinked system. The sandwiched configuration (S) exhibits a smaller decrease in its ionic conductivity, while the parallel displaced (PD) configuration remains constant. The pore spacing of both systems decreases upon crosslinking. The vertical distance between stacked monomers increases in the sandwiched configuration and decreases in the parallel displaced configuration. The correlation length decreases in both configurations.

which do not fit the experimental profile we have tried to match. We explored two classes of metastable basins which are dependent on the initial vertical stacking distance between monomers: the ordered and disordered pore basins. We expect that these metastable configurations will eventually rearrange and converge to a single equilibrium structure. We conducted extensive analysis in order to isolate structures which most closely resemble the true equilibrium structure.

We achieve maximum structural consistency with experiment, as determined by simu-

lated 2D XRD patterns, when we build our model in the ordered basin parallel displaced configuration with 5 monomer columns per pore and 1 wt% water. R-alkanes and R-pores appear where expected for the reasons originally predicted. We find that R-spots is likely due to ordered alkane chain packing. R- $\pi$  appears at lower q values than experiment because monomer stack too far apart, and its intensity is far too high, likely because our initial configurations contain a high level of dependence between monomer columns. We can learn more about the time averaged structure of these systems by studying ensembles of independent simulations. Finally, we observed that our model can only produce R-double when we add small amounts of water to the system. This observation has possible implications for the reproducibility of the experimental results from Feng et al. since they claim that their membrane is completely dry.

We characterized the environment centered around the membrane pores and learned that the pores are generally filled with monomer head groups and sodium ions. All dry systems studied showed a similar distribution of sodium, head groups and tails while the wet system shows evidence of slight swelling, with minor changes in the distributions due to the presence of water molecules. We also observed that there is not a hard partition between hydrophilic and hydrophobic regions; instead, there is a gradient of chemical constituents. This finding raises questions about the nature of size-exclusion separations in systems without a well-defined pore size, which potentially could enable separations that vary with chemical identity as well as size.

Our system can reasonably estimate ionic conductivity. Our calculations are about 1 order of magnitude higher than experiment, however that is to be expected since we are simulating a perfectly straight and defect-free membrane.

Finally, we verified that our conclusions do not change when the system is cross-linked by the algorithm we implemented. The diffraction pattern weakens relative to the uncross-linked system, ionic conductivity drops by a factor of ca. 1.5, in closer agreement with experiment, the pore spacing decreases and the membrane becomes thicker; however, all

changes are relatively minor, preserving most of the features well.

Future work, based on what has been learned in this study, may help further improve the structural agreement between experiment and simulation. Force fields explicitly including  $\pi - \pi$  interactions may be able to draw stacked monomers closer together. We can study ensembles of long simulations in order to observe more averaged structure and to create more experimentally consistent XRD patterns. Extremely long simulations (on the order of  $\mu\text{s}$ ) may be necessary to better quantify the time scales for large scale rearrangements, and the precise arrangements themselves.

With the structural understanding gained by these simulations, it will be possible to evaluate transport of various solutes within the system, and apply the knowledge gained from this study in order to suggest improvements to the existing system, as well as to evaluate new unsynthesized LLC systems.

## References

- (1) Fritzmann, C.; Lwenberg, J.; Wintgens, T.; Melin, T. State-of-the-Art of Reverse Osmosis Desalination. *Desalination* **2007**, *216*, 1–76.
- (2) Schwarzenbach, R. P.; Escher, B. I.; Fenner, K.; Hofstetter, T. B.; Johnson, C. A.; Gunten, U. v.; Wehrli, B. The Challenge of Micropollutants in Aquatic Systems. *Science* **2006**, *313*, 1072–1077.
- (3) Werber, J. R.; Osuji, C. O.; Elimelech, M. Materials for Next-Generation Desalination and Water Purification Membranes. *Nat. Rev. Mater.* **2016**, *1*, 16018.
- (4) Dischinger, S. M.; Rosenblum, J.; Noble, R. D.; Gin, D. L.; Linden, K. G. Application of a Lyotropic Liquid Crystal Nanofiltration Membrane for Hydraulic Fracturing Flowback Water: Selectivity and Implications for Treatment. *J. Membr. Sci.* **2017**, *543*, 319–327.
- (5) Van Der Bruggen, B.; Vandecasteele, C.; Van Gestel, T.; Doyen, W.; Leysen, R. A Review of Pressure-Driven Membrane Processes in Wastewater Treatment and Drinking Water Production. *Environ. Prog.* **2003**, *22*, 46–56.
- (6) Humplik, T.; Lee, J.; OHern, S. C.; Fellman, B. A.; Baig, M. A.; Hassan, S. F.; Atieh, M. A.; Rahman, F.; Laoui, T.; Karnik, R. et al. Nanostructured Materials for Water Desalination. *Nanotechnology* **2011**, *22*, 292001.
- (7) Cohen-Tanugi, D.; Lin, L.-C.; Grossman, J. Multilayer Nanoporous Graphene Membranes for Water Desalination. *Nano Lett.* **2016**, *16*, 1027–1033.
- (8) Hata, K.; Futaba, D. N.; Mizuno, K.; Namai, T.; Yumura, M.; Iijima, S. Water-Assisted Highly Efficient Synthesis of Impurity-Free Single-Walled Carbon Nanotubes. *Science* **2004**, *306*, 1362–1364.
- (9) Maruyama, S.; Einarsson, E.; Murakami, Y.; Edamura, T. Growth Process of Vertically Aligned Single-Walled Carbon Nanotubes. *Chem. Phys. Lett.* **2005**, *403*, 320–323.

- (10) Smith, R. C.; Fischer, W. M.; Gin, D. L. Ordered Poly(p-phenylenevinylene) Matrix Nanocomposites via Lyotropic Liquid-Crystalline Monomers. *J. Am. Chem. Soc.* **1997**, *119*, 4092–4093.
- (11) Zhou, M.; Kidd, T. J.; Noble, R. D.; Gin, D. L. Supported Lyotropic Liquid-Crystal Polymer Membranes: Promising Materials for Molecular-Size-Selective Aqueous Nanofiltration. *Adv. Mater.* **2005**, *17*, 1850–1853.
- (12) Donnan, F. G. Theory of Membrane Equilibria and Membrane Potentials in the Presence of Non-Dialysing Electrolytes. a Contribution to Physical-Chemical Physiology. *J. Membr. Sci.* **1995**, *100*, 45–55.
- (13) Hatakeyama, E. S.; Gabriel, C. J.; Wiesnauer, B. R.; Lohr, J. L.; Zhou, M.; Noble, R. D.; Gin, D. L. Water Filtration Performance of a Lyotropic Liquid Crystal Polymer Membrane with Uniform, Sub-1-Nm Pores. *J. Membr. Sci.* **2011**, *366*, 62–72.
- (14) Hatakeyama, E. S.; Wiesnauer, B. R.; Gabriel, C. J.; Noble, R. D.; Gin, D. L. Nanoporous, Bicontinuous Cubic Lyotropic Liquid Crystal Networks via Polymerizable Gemini Ammonium Surfactants. *Chem. Mater.* **2010**, *22*, 4525–4527.
- (15) Carter, B. M.; Wiesnauer, B. R.; Hatakeyama, E. S.; Barton, J. L.; Noble, R. D.; Gin, D. L. Glycerol-Based Bicontinuous Cubic Lyotropic Liquid Crystal Monomer System for the Fabrication of Thin-Film Membranes with Uniform Nanopores. *Chem. Mater.* **2012**, *24*, 4005–4007.
- (16) Feng, X.; Tousley, M. E.; Cowan, M. G.; Wiesnauer, B. R.; Nejati, S.; Choo, Y.; Noble, R. D.; Elimelech, M.; Gin, D. L.; Osuji, C. O. Scalable Fabrication of Polymer Membranes with Vertically Aligned 1 nm Pores by Magnetic Field Directed Self-Assembly. *ACS Nano* **2014**, *8*, 11977–11986.
- (17) Matyka, M.; Khalili, A.; Koza, Z. Tortuosity-Porosity Relation in Porous Media Flow. *Phys. Rev. E* **2008**, *78*, 026306.

- (18) Zhou, M.; Nemade, P. R.; Lu, X.; Zeng, X.; Hatakeyama, E. S.; Noble, R. D.; Gin, D. L. New Type of Membrane Material for Water Desalination Based on a Cross-Linked Bicontinuous Cubic Lyotropic Liquid Crystal Assembly. *J. Am. Chem. Soc.* **2007**, *129*, 9574–9575.
- (19) Feng, X.; Nejati, S.; Cowan, M. G.; Tousley, M. E.; Wiesnauer, B. R.; Noble, R. D.; Elimelech, M.; Gin, D. L.; Osuji, C. O. Thin Polymer Films with Continuous Vertically Aligned 1 nm Pores Fabricated by Soft Confinement. *ACS Nano* **2016**, *10*, 150–158.
- (20) Dischinger, S. M.; McGrath, M. J.; Bourland, K. R.; Noble, R. D.; Gin, D. L. Effect of Post-Polymerization Anion-Exchange on the Rejection of Uncharged Aqueous Solutes in Nanoporous, Ionic, Lyotropic Liquid Crystal Polymer Membranes. *J. Membr. Sci.* **2017**, *529*, 72–79.
- (21) Resel, R.; Leising, G.; Markart, P.; Kriegbaum, M.; Smith, R.; Gin, D. Structural properties of polymerised lyotropic liquid crystals phases of 3,4,5-tris(-acryloxyalkoxy)benzoate salts. *Macromol. Chem. Phys.* **2000**, *201*, 1128–1133.
- (22) McIntosh, T. J.; Simon, S. A.; MacDonald, R. C. The Organization of N-Alkanes in Lipid Bilayers. *Biochim. Biophys. Acta, Biomembr.* **1980**, *597*, 445–463.
- (23) Govind, A. S.; Madhusudana, N. V. A Simple Molecular Theory of Smectic-C Liquid Crystals. *EPL* **2001**, *55*, 505.
- (24) Zhu, X.; Scherbina, M. A.; Bakirov, A. V.; Gorzolnik, B.; Chvalun, S. N.; Beginn, U.; Müller, M. Methacrylated Self-Organizing 2,3,4-Tris(alkoxy)benzenesulfonate: A New Concept Toward Ion-Selective Membranes. *Chem. Mater.* **2006**, *18*, 4667–4673.
- (25) Chaikin, P.; Lubensky, T. *Principles of Condensed Matter Physics*, 1st ed.; Cambridge University Press: Cambridge, UK, 1995.

- (26) Wang, J.; Wolf, R. M.; Caldwell, J. W.; Kollman, P. A.; Case, D. A. Development and Testing of a General Amber Force Field. *J. Comput. Chem.* **2004**, *25*, 1157–1174.
- (27) Wang, J.; Wang, W.; Kollman, P. A.; Case, D. A. Automatic Atom Type and Bond Type Perception in Molecular Mechanical Calculations. *J. Mol. Graphics. Modell.* **2006**, *25*, 247–260.
- (28) Case, D.; Betz, R.; Botello-Smith, W.; Cerutti, D.; Cheatham, T., III; Darden, T.; Duke, R.; Giese, T.; Gohlke, H.; Goetz, A. et al. AmberTools16. 2016.
- (29) Bekker, H.; Berendsen, H. J. C.; Dijkstra, E. J.; Achterop, S.; van Drunen, R.; van der Spoel, D.; Sijbers, A.; Keegstra, H.; Reitsma, B.; Renardus, M. K. R. GROMACS: A Parallel Computer for Molecular Dynamics Simulations. Physics Computing '92 ed. 1993.
- (30) Berendsen, H. J. C.; van der Spoel, D.; van Drunen, R. GROMACS: A Message-Passing Parallel Molecular Dynamics Implementation. *Comput. Phys. Commun.* **1995**, *91*, 43–56.
- (31) Van Der Spoel, D.; Lindahl, E.; Hess, B.; Groenhof, G.; Mark, A. E.; Berendsen, H. J. C. GROMACS: Fast, Flexible, and Free. *J. Comput. Chem.* **2005**, *26*, 1701–1718.
- (32) Hess, B.; Kutzner, C.; van der Spoel, D.; Lindahl, E. GROMACS 4: Algorithms for Highly Efficient, Load-Balanced, and Scalable Molecular Simulation. *J. Chem. Theory Comput.* **2008**, *4*, 435–447.
- (33) Mondal, J.; Mahanthappa, M.; Yethiraj, A. Self-Assembly of Gemini Surfactants: A Computer Simulation Study. *J. Phys. Chem. B* **2013**, *117*, 4254–4262.
- (34) Martnez, L.; Andrade, R.; Birgin, E. G.; Martnez, J. M. Packmol: A Package for Building Initial Configurations for Molecular Dynamics Simulations. *J. Comput. Chem.* **2009**, *30*, 2157–2164.

- (35) Sinnokrot, M. O.; Valeev, E. F.; Sherrill, C. D. Estimates of the Ab Initio Limit for Interactions: The Benzene Dimer. *J. Am. Chem. Soc.* **2002**, *124*, 10887–10893.
- (36) Chodera, J. D. A Simple Method for Automated Equilibration Detection in Molecular Simulations. *J. Chem. Theory Comput.* **2016**, *12*, 1799–1805.
- (37) Kuriabova, T.; Betterton, M. D.; Glaser, M. A. Linear Aggregation and Liquid-Crystalline Order: Comparison of Monte Carlo Simulation and Analytic Theory. *J. Mater. Chem.* **2010**, *20*, 10366–10383.
- (38) Slater, J. C. Atomic Radii in Crystals. *J. Chem. Phys.* **1964**, *41*, 3199–3204.
- (39) Oliphant, T. E. Python for Scientific Computing. *Comput. Sci. Eng.* **2007**, *9*, 10–20.
- (40) Einstein, A. *Investigations on the Theory of the Brownian Movement*; Dover Publications: Dover, New York, USA, 1956.
- (41) Caleman, C.; van Maaren, P. J.; Hong, M.; Hub, J. S.; Costa, L. T.; van der Spoel, D. Force Field Benchmark of Organic Liquids: Density, Enthalpy of Vaporization, Heat Capacities, Surface Tension, Isothermal Compressibility, Volumetric Expansion Coefficient, and Dielectric Constant. *J. Chem. Theory Comput.* **2012**, *8*, 61–74.
- (42) Wang, L.-P.; McKiernan, K. A.; Gomes, J.; Beauchamp, K. A.; Head-Gordon, T.; Rice, J. E.; Swope, W. C.; Martnez, T. J.; Pande, V. S. Building a More Predictive Protein Force Field: A Systematic and Reproducible Route to AMBER-FB15. *J. Phys. Chem. B* **2017**, *121*, 4023–4039.
- (43) Harburn, G.; Taylor, C. A.; Welberry, T. R. *Atlas of Optical Transforms*; Cornell University Press: Ithaca, New York, USA, 1975; Google-Books-ID: BwCFAAAIAAJ.
- (44) Taylor, G. The Phase Problem. *Acta Cryst D* **2003**, *59*, 1881–1890.
- (45) Carey, F.; Giuliano, R. *Organic Chemistry*, 8th ed.; McGraw-Hill Companies, Inc.: USA, 2011.

- (46) Tauer, T. P.; Sherrill, C. D. Beyond the Benzene Dimer: An Investigation of the Additivity of Interactions. *J. Phys. Chem. A* **2005**, *109*, 10475–10478.
- (47) Dong, R. Y.; Goldfarb, D.; Moseley, M. E.; Luz, Z.; Zimmermann, H. Translational Diffusion in Discotic Mesophases Studied by the Nuclear Magnetic Resonance Pulsed Field Gradient Method. *J. Phys. Chem.* **1984**, *88*, 3148–3152.
- (48) Dvinskikh, S. V.; Fur, I.; Zimmermann, H.; Maliniak, A. Molecular Self-Diffusion in a Columnar Liquid Crystalline Phase Determined by Deuterium NMR. *Phys. Rev. E* **2002**, *65*, 050702.
- (49) Liu, Y.; Zhu, F. Collective Diffusion Model for Ion Conduction Through Microscopic Channels. *Biophys. J.* **2013**, *104*, 368–376.

## Graphical TOC Entry

